AFRL-ML-WP-TR-1999-4010

EXPLORATORY NONDESTRUCTIVE
EVALUATION (NDE) RESEARCH FOR
ADVANCED MATERIALS AND PROCESSES

VOLUME 2 : SHEAROGRAPHY
IMPROVEMENTS

RICHARD BOSSI   LYLE DEOBALD
BENJAMIN KNUTSON   JAMES NELSON
ROBERT NERENBERG   WILLIAM SHEPHERD

BOEING INFORMATION
SPACE & DEFENSE SYSTEMS
P.O.BOX 3999
SEATTLE, WA 98124

JULY 1998

FINAL REPORT FOR 07/01/1995 – 04/30/1998

APPROVED FOR PUBLIC RELEASE; DISTRIBUTION UNLIMITED

19990715 036

MATERIALS AND MANUFACUTURING DIRECTORATE
AIR FORCE RESEARCH LABORATORY
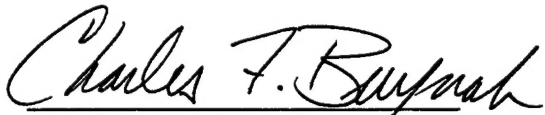AIR FORCE MATERIEL COMMAND
WRIGHT-PATTERSON AIR FORCE BASE OH 45433-7734

DTIC QUALITY INSPECTED 4

NOTICE

WHEN GOVERNMENT DRAWINGS, SPECIFICATIONS, OR OTHER DATA ARE USED FOR ANY PURPOSE OTHER THAN IN CONNECTION WITH A DEFINITELY GOVERNMENT-RELATED PROCUREMENT, THE UNITED STATES GOVERNMENT INCURS NO RESPONSIBILITY OR ANY OBLIGATION WHATSOEVER. THE FACT THAT THE GOVERNMENT MAY HAVE FORMULATED OR IN ANY WAY SUPPLIED THE SAID DRAWINGS, SPECIFICATIONS, OR OTHER DATA, IS NOT TO BE REGARDED BY IMPLICATION OR OTHERWISE IN ANY MANNER CONSTRUED, AS LICENSING THE HOLDER OR ANY OTHER PERSON OR CORPORATION, OR AS CONVEYING ANY RIGHTS OR PERMISSION TO MANUFACTURE, USE, OR SELL ANY PATENTED INVENTION THAT MAY IN ANY WAY BE RELATED THERETO.

THIS REPORT IS RELEASABLE TO THE NATIONAL TECHNICAL INFORMATION SERVICE (NTIS). AT NTIS, IT WILL BE AVAILABLE TO THE GENERAL PUBLIC, INCLUDING FOREIGN NATIONS.

THIS TECHNICAL REPORT HAS BEEN REVIEWED AND IS APPROVED FOR PUBLICATION.

CHARLES F. BUYNAK, Project Engineer
Nondestructive Evaluations Branch
Metals, Ceramics & NDE Division

THOMAS J. MORAN, Acting Chief
Nondestructive Evaluations Branch
Metals, Ceramics & NDE Division

GERALD J. PETRAK, Assistant Chief
Metals, Ceramics & NDE Division
Materials & Manufacturing Directorate

REPORT DOCUMENTATION PAGE

Form Approved
OMB No. 0704-0188

1. AGENCY USE ONLY *(Leave blank)*	2. REPORT DATE	3. REPORT TYPE AND DATES COVERED
	JULY 1998	FINAL REPORT FOR 07/01/1995 - 04/30/1998

4. TITLE AND SUBTITLE
EXPLORATORY NONDESTRUCTIVE EVALUATION (NDE) RESEARCH FOR ADVANCED MATERIALS AND PROCESSES; VOLUME 2 : SHEAROGRAPHY IMPROVEMENTS

5. FUNDING NUMBERS
C   F33615-95-C-5225
PE   62102
PR   4349
TA   44
WU   01

6. AUTHOR(S)
RICHARD BOSSI, LYLE DEOBALD, BENJAMIN KNUTSON, JAMES NELSON, ROBERT NERENBERG, AND WILLIAM SHEPHERD

7. PERFORMING ORGANIZATION NAME(S) AND ADDRESS(ES)
BOEING INFORMATION
SPACE & DEFENSE SYSTEMS
P.O.BOX 3999
SEATTLE, WA 98124

8. PERFORMING ORGANIZATION REPORT NUMBER

D950-10333-1

9. SPONSORING/MONITORING AGENCY NAME(S) AND ADDRESS(ES)
MATERIALS AND MANUFACTURING DIRECTORATE
AIR FORCE RESEARCH LABORATORY
AIR FORCE MATERIEL COMMAND
WRIGHT-PATTERSON AFB, OH 45433- 7734
POC: CHARLES F. BUYNAK, AFRL/MLLP, 937-255-9807

10. SPONSORING/MONITORING AGENCY REPORT NUMBER

AFRL-ML-WP-TR-1999-4010

11. SUPPLEMENTARY NOTES

12a. DISTRIBUTION AVAILABILITY STATEMENT
APPROVED FOR PUBLIC RELEASE, DISTRIBUTION UNLIMITED

12b. DISTRIBUTION CODE

13. ABSTRACT *(Maximum 200 words)*
Shearography Improvements: Shearographic inspection of aerospace structures has not gained wide acceptance, owing to the difficulty of interpreting shearographic images. A feature extraction method was developed that calculates surface normal curvature from input shearograms. The method can be applied in real time to provide a technician unambiguous images representing areas of locally high curvature, which will generally highlight the boundaries of flaws.
Images are load independent and insensitive to part viewing angle. Analytical and experimental validation tests were completed for vacuum, vibrational and thermal loading. Recommendations are presented for system development, and for practical implementation of shearography

14. SUBJECT TERMS
Failure Analysis, X-ray, Imaging, Microfocus, Radioscopy, Computed Tomography, Electronics, Composites, Area Inspection, Shearography, Interactive Multimedia Based Training, Computer-Managed Instruction, Nondestructive Evaluation and Inspection

15. NUMBER OF PAGES
50

16. PRICE CODE

17. SECURITY CLASSIFICATION OF REPORT	18. SECURITY CLASSIFICATION OF THIS PAGE	19. SECURITY CLASSIFICATION OF ABSTRACT	20. LIMITATION OF ABSTRACT
UNCLASSIFIED	UNCLASSIFIED	UNCLASSIFIED	SAR

Standard Form 298 (Rev. 2-89) (EG)
Prescribed by ANSI Std. 239.18
Designed using Perform Pro, WHS/DIOR, Oct 94

TABLE OF CONTENTS

LIST OF FIGURES

LIST OF TABLES

ACKNOWLEDGEMENTS

DISCLAIMER

EXECUTIVE SUMMARY

Boeing Defense & Space Group was awarded the "Exploratory Nondestructive Evaluation (NDE) Research for Advanced Materials and Processes" contract in 1995 to study improvements for NDE methods for evaluating aging assets, primarily aircraft, with the primary end objective to reduce the cost of maintaining these aging assets.

The study involved three separate approaches, responsive to the three task elements contained in the Statement of Work. The first approach was to look at the use of high resolution computed tomography (CT) in failure analysis, the second was to study improvements in shearography, and the third was a demonstration of the use of interactive multimedia computer-based training for NDE/I inspectors. Because each task is distinctly unique, they are discussed in separate report volumes – collectively referred to as FAST: Failure Analysis, Shearography, Training. This is volume 2, covering Shearography.

Point-by-point NDI methods, such as ultrasonic or eddy current are prohibitively expensive for the large area screening inspections required to identify suspect damage areas in aerospace structures so that maintenance actions can be undertaken in a timely and cost effective manner. Visual inspections are commonly used today for area inspection because of their relative simplicity. However, visual inspection does not discriminate failure modes whose first indication may be exposed surface displacements on the order of a few wavelengths of light. Shearography offers a large area inspection methodology that can provide early detection of void formation in structures when employed with appropriate excitation methods such as vacuum-, thermal-, or vibration-loading.

Shearography is an optical imaging technology based on speckle interferometry that has been under practical development since the mid-70's. It does not require a precisely aligned and stable platform. However, shearography has not gained general acceptance as an inspection technique because of present difficulty of fringe interpretation. Its effectiveness depends on the subjective evaluation by a technician, and interpretation can vary considerably from one practitioner to the next.

For shearography to become a reliable method for large area inspection of aircraft and aerospace assemblies, the requirement for subjective evaluation by a skilled operator must be reduced. Our primary goal has been development of a platform and geometry independent method for interpretation of shearographic data, which will enable the cost benefits of shearographic inspection to be realized in Air Force maintenance practice. Further objectives have been to identify and recommend needed improvements to shearographic test equipment, and to evaluate quantitative measurement, and data processing methodologies.

A feature extraction methodology, "NCOS" (for Normalized Curvature from Orthogonal Shearograms), was developed that is applicable to real-time display of processed images derived from speckle shearograms. The processed images show local, normalized curvature and greatly reduce the present ambiguity of interpretation associated with the raw input images. The method, which relies on computation of normalized curvature by appropriate differentiation of information encoded in orthogonal shearograms, is not affected by part

1

orientation, or the viewing aspect of the shearing camera. The only effect of off-normal viewing is apparent perspective distortion familiar in normal vision.

The computational method was developed and refined with the aid of predictive displacement models for several loading methods applied to a debond phantom fabricated for this program. The models were combined with synthetic shearography codes that were used to support development of the NCOS algorithm.

A baseline, two-camera measurement geometry was tested for simultaneous acquisition of orthogonal shearograms. Lessons learned from the use of this system provide the basis for implementation of a compact, fieldable system taking advantage of the feature extraction methods developed. An advanced system design can be proposed which resolves several deficiencies in currently available shearographic instruments identified as a result of this work. Simultaneous acquisition of unrectified, orthogonal shearograms, based on 12-to-16 bit images, will permit optimized real-time display of NCOS reduced raw data that can unambiguously localize unbonded regions of areas being inspected. Fidelity similar to that demonstrated by model calculations using the "Bird Strike" disbond distribution during this work can be expected in practical inspection environments.

1.0 INTRODUCTION

Boeing is pleased to submit this final report on the work to improve the interpretability of shearographic NDT data performed under contract F33615-95-C-5225, entitled "NDE for Aging Aircraft Service Life Prediction". Our primary goal on this task has been development of a platform and geometry independent method for interpretation of shearographic data, which will enable the cost benefits of shearographic inspection to be realized in Air Force maintenance practice. For shearography to become a reliable method for large area inspection of aircraft and aerospace assemblies, the requirement for subjective evaluation by a skilled operator must be reduced. Further objectives have been to identify and recommend needed improvements to shearographic test equipment, and to evaluate quantitative measurement, and data processing methodologies.

1.1 Background

Life extension programs for military systems are becoming increasingly important as defense budgets shrink and world economies realign themselves to an uncertain future. Military systems are being required to operate many years beyond their original design lifetimes. NDE/I is an essential element for accomplishing this cost control effectively while maintaining an acceptable level of safety and functionality. Point-by-point NDI methods, such as ultrasonic or eddy current are prohibitively expensive for the large area screening inspections required to identify suspect areas so that maintenance actions can be undertaken in a timely and cost effective manner. Visual inspections are commonly used today for area inspection because of their relative simplicity. However, visual inspection does not discriminate failure modes, its first indication may be exposed surface displacements on the order of a few wavelengths of light. Shearography offers a large area inspection methodology that can provide early detection of void formation in structures (debonds, failed fastening systems) when employed with appropriate excitation methods such as vacuum-, thermal-, or vibration-loading. Shearography is an optical imaging technology based on speckle interferometry that has been under practical development since the mid-70's. It differs from other interferographic methods in that it is relatively insensitive to part vibration, and whole body motion. It does not require a precisely aligned and stable platform. Shearography produces relatively low fringe contrast in the interferograms, since they exist only as a consequence of speckle.

Shearography has not gained general acceptance as an inspection technique because of present difficulty of fringe interpretation. Figure 1.1 shows a classic shearogram resulting from slight deformation of a thin diaphragm owing to vibrational loading (maximum surface displacement is on the order of a few wavelengths of blue-green light). One observes an easily recognized "butterfly pattern" associated with this case. It is clear in the figure that fringe contrast is low owing to the presence of speckle, but the pattern is obvious to the eye, and clearly marks the defect. Figures 1.2(a) and (b) show two shearograms generated from multiple elongated disbonds in a composite part being vacuum loaded. The shearing axis is vertical in (a) and horizontal in (b). The defects are nearly impossible to recognize in (a), and difficult to localize in (b). Figures 1.3(a) and (c) show orthogonal shearograms generated synthetically from the distribution of defects shown in Figure 1.3(b). Here, the

3

simulated disbonds are reasonably well localized, but the shearogram is nearly indecipherable as it stands, even in the absense of speckle. These three figures demonstrate the principal difficulty for routine application of shearography. As defect structures become more complex, shearograms become increasngly difficult to interpret. Relatively isolated defect clusters, which might not require repair, produce widely dispersed fringe patterns suggestive of much more serious defects, if they can be recognized at all. The utility of shearography then depends on the subjective evaluation by a technician, and interpretation can vary considerably from one practitioner to the next.

(a)   (b)
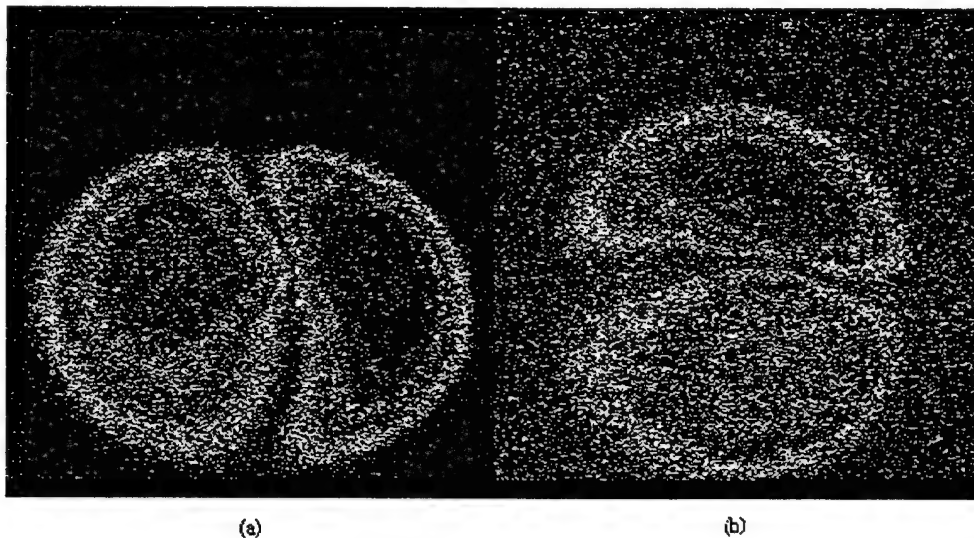
Figure 1.1.   Measured shearograms from vibrationally loaded, circular diaphragm illustrating a classic butterfly pattern

(a)   (b)
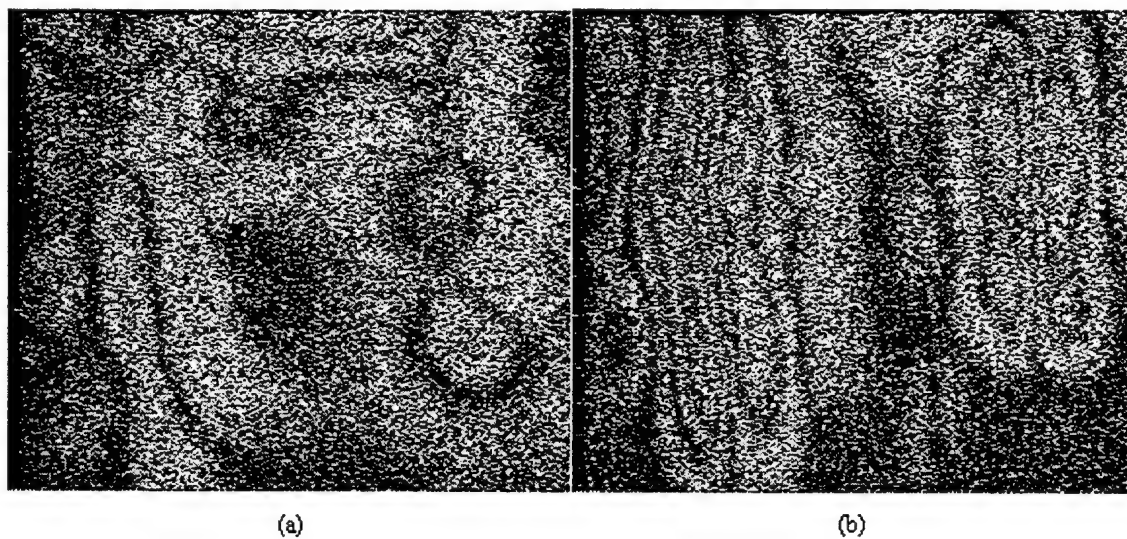
Figure 1.2.   Shearograms obtained from a vacuum loaded 767 composite spoiler panel having multiple, neighboring debonds

4
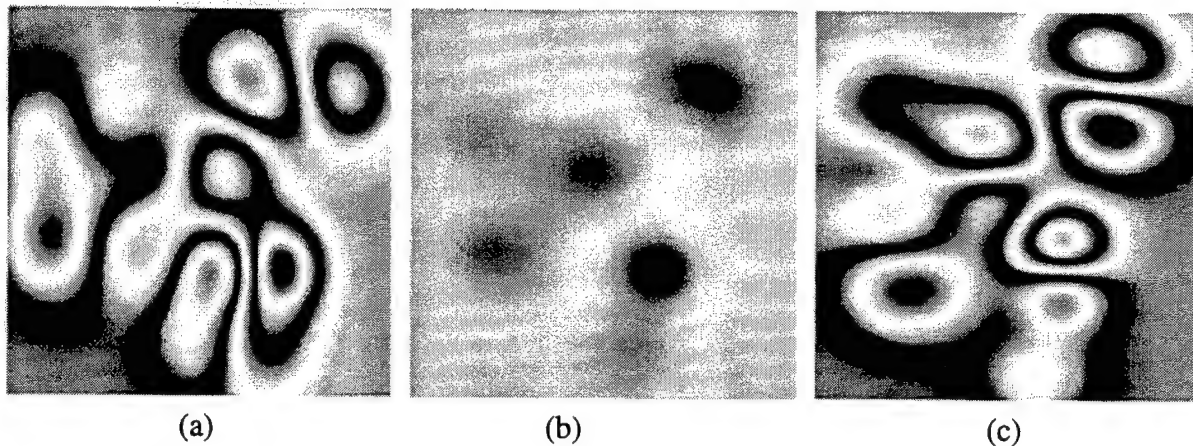
Figure 1.3.   Synthetic shearograms obtained from a complex of simulated debonds. (a) X-axis shearogram; (b) curvature image calculated from the input displacement; (c) Y-axis shearogram

The work reported here was undertaken to develop methods for evaluating shearograms that reduce subjectivity of interpretation.   This is a necessary and important precursor to preparation of a Technical Order to authorize shearographic inspection for routine application at maintenance depots.

Methods developed rely on the fact that sensitivity to localized changes in part surfaces as a result that applied loading is generally enhanced by differentiation of the observed response. Much of the past work of others focused on integration of the observed part response to recover surface displacement. Differentiation emphasizes areas having a high rate-of-change of slope and its derivatives, while de-emphasizing large scale change such as rigid body motion and large scale bending.   The latter contains information extraneous to defect localization, and tends to be obscuring.   It is also important that methods for defect recognition be insensitive to viewing geometry so that defects can be found from arbitrary viewing angles, and on curved surfaces that may present indications that are not aligned with the viewing system.   This objective is met by the use of a scalar operator for feature extraction.   In this work, estimation of the Laplacian of the axial displacement field was chosen for development.   The Laplacian of the displacement field is the surface curvature. Local curvature is numerically related to the radius of a tangent sphere, being proportional to one over the square of its radius.   Since, in nearly all cases, curvature is maximized near the pinned boundaries of defects, this approach can be expected to outline defect edges, facilitating localization.   This attribute makes it possible to extract information about defect size, connectivity, and morphology from shearographic images that otherwise cannot be directly interpreted.   Additionally, normalization of the extracted curvature data produces a load independent outcome for those cases where the structural deformation is linear (as is the case for the small displacements necessary to produce measurable shearographic indications). This means that shearograms processed as described will have the same appearance regardless of specific excitation conditions.   The algorithm developed for implementation of the curvature extraction methodology is referred to, in the following, as "NCOS" (for Normalized Curvature from Orthogonal Shearograms).

5

2.0 PROGRAM DESCRIPTION

Shearograms encode one component of the gradient of displacement, corresponding to the direction in which the sheared images are displaced. Differentiation of displacement with respect to position in the shearing direction to yield this surface gradient component is accomplished optically, and is, therefore, "exact" (not subject to the approximations of numerical differentiation). The Laplacian is formed by numerically differentiating the optically produced derivative with respect to the same shearing direction, and adding the result to the corresponding quantity obtained from a second, orthogonally sheared interferogram. The second derivatives are subject to a number of numerical approximations, and data representation artifacts. The details of the method are discussed in the following. Wherever the term differentiation is used below, it is with respect to position in the shearing direction unless otherwise noted.

2.1 Shearogram Formation

Formation and interpretation of speckle shearograms is discussed by Hung, et al.[1]. Electronic speckle shearograms result from calculating the pixel-by-pixel difference between electronic speckle pattern interferograms (ESPI's) obtained before and after part excitation. An ESPI is obtained by interfering a speckle image of a part with its slightly displaced (sheared) image produced, in principle, by passing a portion of laser light scattered from the part surface through a wedge before combining the two on a recording medium. Typical wedge angles are 0.25-to-2 degrees. Actual implementations often use more sophisticated shearing optics to produce equal and opposite shearing displacements of the two components. The interference patterns produced in this manner have a very high spatial frequency, and do not result in directly observable fringes. No defect information is recoverable from a single ESPI. Subtraction of the two ESPI's does result in fringes containing defect information. For static displacement of the excited surface (e.g., when the part is loaded thermally or by static pressure), the locus of observed fringes is a sinusoidally modulated measure of the axial displacement gradient component, in the shearing direction. The gradient component being modulated is scaled by a constant representing the geometry of the measurement and the characteristics of the shearing camera.

From Hung, the optical phase shift, $\Delta\phi_x$, produced by a surface gradient in the x direction is given by:

$$\Delta\Phi_x = \frac{-2\pi}{\lambda}\left[(1+\cos\theta)\frac{\partial w}{\partial x} + (\sin\theta)\frac{\partial u}{\partial x}\right]\Delta x \qquad (1)$$

where θ is the angle between the illuminating and viewing directions, Δx is the displacement of the two image contributions relative to each other, and the gradient of interest is $\delta w/\delta x$. λ is the illuminating wave length. $\Delta x = S*\alpha$, where α is the shearing angle in radians and S is the distance from the camera to the part. The surface normal component of displacement is w, and, in the approximation of small displacements, u (the x component) and v (the y

6

component) are negligible. For simplicity in this discussion, we assume that the camera and illuminator are collocated, in which case θ = 0, and

$$\Delta\Phi_x = -\frac{4\pi}{\lambda}\frac{\partial w}{\partial x}S\alpha \qquad (2)$$

Similar expressions (with x replaced by y) apply for shearing in the y direction.

The fringe pattern resulting from this phase term has an intensity modulation given by:

$$I_x = 4a^2\sin(\phi+\Delta\phi)\sin\left(\frac{\Delta\phi_x}{2}\right) \qquad (3)$$

This describes a rapidly varying intensity term on a scale generally smaller than a resolution element, modulated by a slowly varying term describing the visual fringe modulation. Null fringes occur when $\Delta\phi_x=2n\pi$ (n integer). This gives a sensitivity for δw/δx:

$$\frac{\partial w}{\partial x} \propto \frac{\lambda}{2S\alpha} \qquad (4)$$

This shows that for typical values of λ, S and α, of 0.535 microns, 1 meter, and 1 degree, respectively, sensitivity is about $1.5*10^{-8}$microns/mm.

2.2 Calculation of the Laplacian

The Laplacian of w is: $\nabla^2 w = \dfrac{\partial^2 w}{\partial x^2} + \dfrac{\partial^2 w}{\partial y^2}$ which is obtained by calculating the respective second partial derivatives from the inverse sine of the experimentally derived intensity modulation. For shearing in x:

$$\frac{\partial w}{\partial x} = \frac{2\lambda\sin^{-1}I_x}{4S\pi\alpha} \qquad (5)$$

$$\frac{\partial^2 w}{\partial x^2} = \frac{\lambda}{2S\pi\alpha}\frac{\partial}{\partial x}\left[\sin^{-1}I_x\right] = \frac{\lambda}{2S\pi\alpha}\left[\frac{1}{\sqrt{1-I_x^2}}\right]\frac{\partial}{\partial x}I_x \qquad (6)$$

The contribution from shear along the y axis is similar. The arcsine function has the fortunate attribute that its derivative is analytic in the range -π/2 to π/2. This avoids numerical problems with principal value ambiguities, and reduces the numerical differentiation problem to a simple derivative over the values stored in the data file. These data are highly modulated because of the presence of speckle, as will be discussed later.

The above formulation applies only when the experimental data are recorded as the simple difference between two ESPI's. It is common to find that commercial shearographic

7

equipment either truncates negative values in the subtraction to zero, or rectifies the difference. In the later case, the measured intensity field is given by the absolute value of the sine, rather than the sine. As a result, there is a sign ambiguity in calculating $\Delta\phi_x$ and $\Delta\phi_y$ that propagates through the steps of the calculation of the Laplacian. An equality cannot be formed between the Laplacian and the second derivatives calculated, as above, from the data. Significant artifacts occur in the calculated curvature image when the two derivatives are summed in any combination of absolute and non-absolute values. While the basic curvature information is recognizable, it is clearly most desirable to obtain, and operate on unrectified data.

2.3 Data Reduction

Calculation of the normalized curvature from shearographic data is the basis for the feature extraction presented here. The steps employed to implement the method are outlined in Figure 2.1. ESPI's are acquired for complementary shearing axes (not necessarily orthogonal) before and after loading. The before-and-after images are subtracted, point-by-point for the two shearing axes and then normalized into the range of the sine function (± 1).

The resultant will be a speckle interferogram representing the locus of points of equal phase shift in the derivative of displacement. The first derivative of displacement is obtained optically and is exact within limits imposed by the resolution elements of the images. The results are spatially filtered to reduce speckle. Second derivatives of displacement are calculated and summed to yield an estimate of the Laplacian. The results are then smoothed to minimize artifacts, which are generated at the limits of the analytic derivative of the arcsine function. Results are normalized, producing a load invariant image that is independent of the specific conditions of the test so long as displacement is linearly related to load. In test cases with simple defect models, curvature is observed to be maximum at the defect boundaries, clearly localizing the affected area. Equalization of the image intensity distribution can be applied when necessary to enhance edge definition in more complex cases.

8
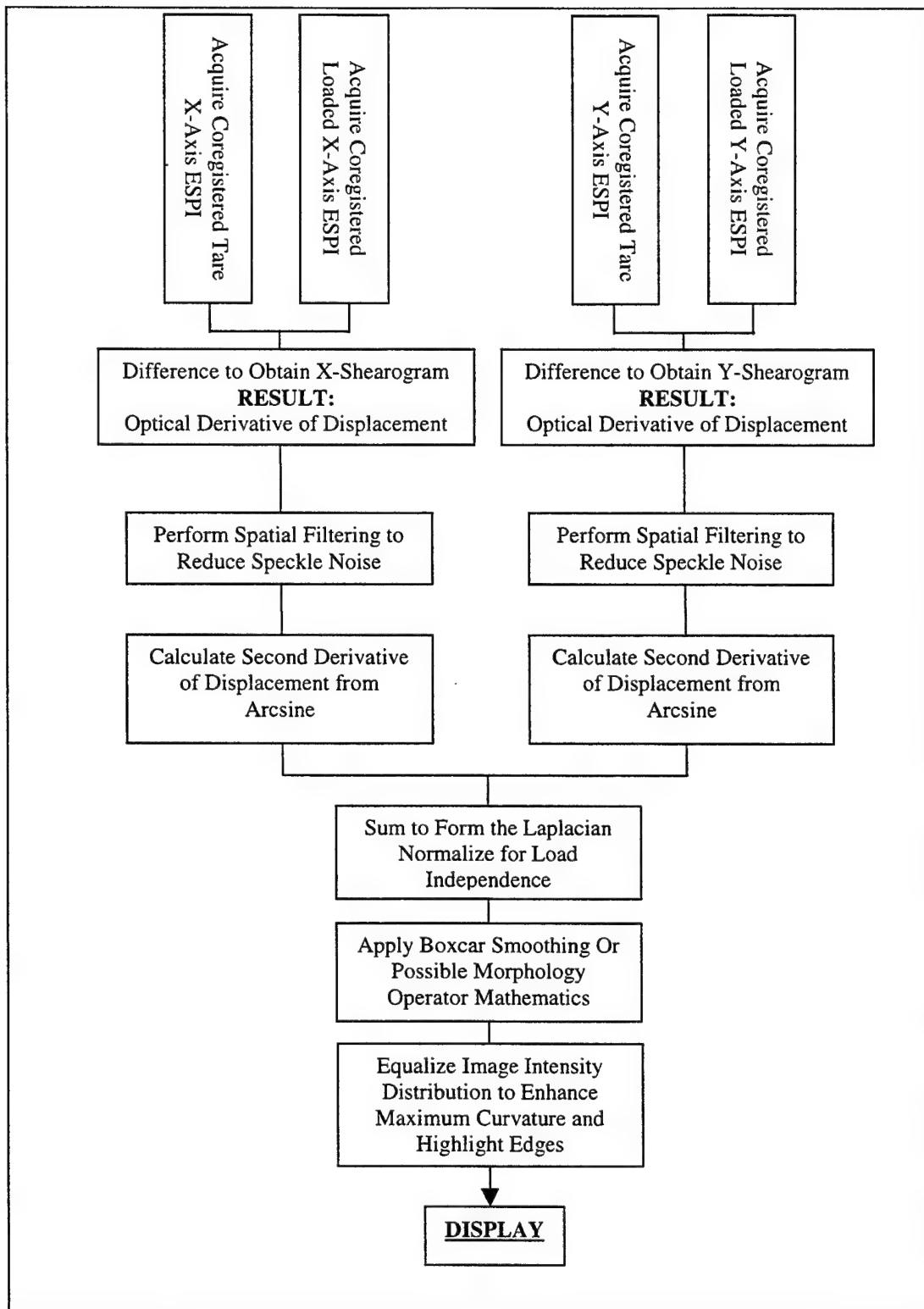
Figure 2.1.   Logic flow of feature extraction methodology

9

2.4 Validation

Development and validation of the NCOS algorithm were carried out, using commercial equipment for shearogram acquisition from multiple sample types, and under a variety of geometric and loading conditions. Analytical development was also supported through use of shearography modeling codes. These included several Boeing developmental codes designed to generate shearograms with continuous speckle, and the Cobra shearographic simulation code, written by Mike Valley at Sandia National Laboratories. Cobra provides a complete shearogram synthesis capability for arbitrarily defined part displacement models. Static and vibrational loading cases can be considered. Shearograms can be synthesized with and without speckle. As presently formulated, Cobra produces rectified shearograms. The Boeing models are convenient for comparing analysis of rectified and unrectified data, and for rapid synthesis and testing of distributed defect models.

Systematic measurements were made using a shearography phantom designed for this effort. A schematic diagram is shown in Figure 2.2. It was fabricated from a nominally two-foot square plate of one-inch thick aluminum. A series of wells were bored in the plate, having diameters of: 0.25, 0.5, 1.0, 1.5, and 2 inches. These wells were bored to leave diaphragms having thicknesses of: 0.01, 0.03, 0.05, 0.07 and 0.09 inches. This geometry represents typical debonds in aerospace structures. Its simple elements are easily modeled, suitable for use in predictive shearography codes such as Cobra. Galleries were machined in the back of the plate to provide for fluid pressurization of the well interiors, when a sealed cover plate was installed. When it was used in this configuration to produce shearograms, pressurization was accomplished by regulating the height of a column of fluid attached to the fluid reservoir. Common antifreeze was used after it was discovered that water rapidly corroded the aluminum, producing gas, which caused rapid pressure drift. Typical applied pressures were 0.1 to 0.5 psi above ambient. This same phantom was used for thermal and vibrational loading tests after the antifreeze was drained and the cover removed.
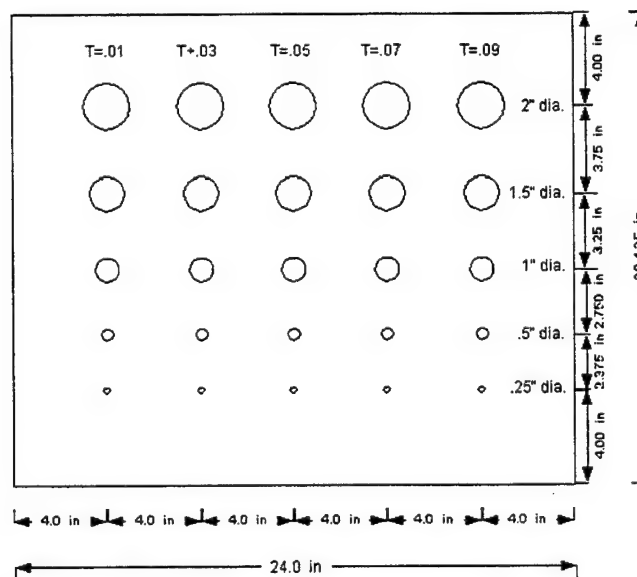
Figure 2.2.   Schematic of Fast debond phantom

2.4.1 Invariance of feature extraction to measurement parameters

An essential property of feature extraction methods for improving interpretation of shearographic images is that they be unaffected by specific viewing conditions. Although the formulation of the NCOS algorithm is discussed above in terms of the surface normal view of the part (for simplicity), off-normal viewing is likely in practical implementations. The Laplacian is a linear scalar operator that has the desired property of view invariance. Curvature images are expected to exhibit the properties of perspective familiar in direct viewing of common objects. The following figures confirm the desired properties of invariance in the NCOS algorithm.

Figure 2.3 shows two instances of NCOS processed shearograms from the debond phantom (above), obtained at normal incidence (a), and at a view angle 37 degrees from normal (b). The phantom was pressurized at 0.17 psi, with a camera standoff distance of 48 inches. The illuminator was mounted on the camera system, and had a small offset from the viewing axis ($\theta \approx 0$). The intensity distributions in the curvature images have been equalized to enhance definition. Note the effect of the tilt is simply foreshortening of the circular defect as would be expected from perspective considerations.

(a)   (b)
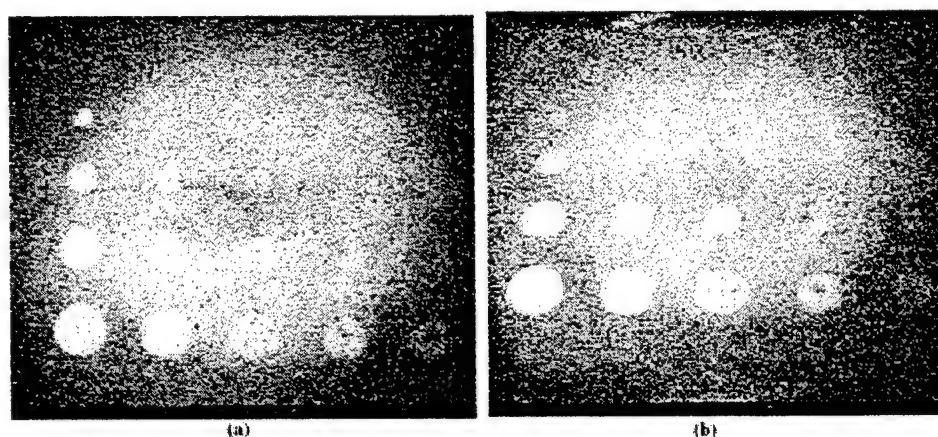
Figure 2.3.   Algorithm performance for oblique shearographic views

Comparison of shearograms obtained at 24" and 48" confirmed the dependence of sensitivity and fringe count on S and α as predicted in equation (4). Additional measurements, taken when the illumination source was offset from the camera, also produced only a reduction in fringe sensitivity according to equation (1).

Figure 2.4 shows the results of NCOS processing when the two contributing shearograms were not obtained for orthogonal shearing directions. Processed data when shearing was in the x-direction were combined with data when shearing was at 45 degrees to the x-axis. The sum of the two contributions does not satisfy the definition of the Laplacian, but the resultant is still a recognizable image with a good approximation to the defect shape. The principal effect of the x-axis contribution from the 45 degree case is to produce skewing along the defect diagonal axis.

11

Processed from orthogonal shearograms   From X-axis + 45 degree shearograms
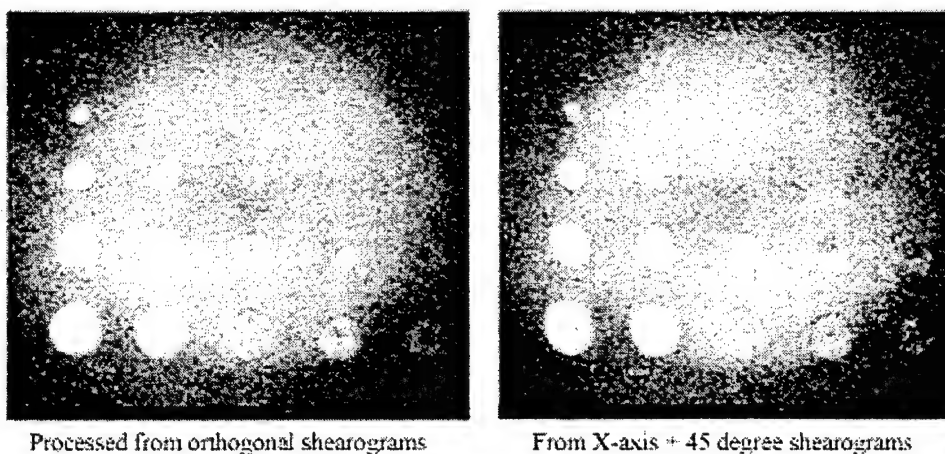
Figure 2.4.   Comparison of curvature images resulting from processing non-orthogonal shearograms

2.4.2 Shearography System Characteristics

Initial measurements were made with an LTI SC4000 portable shearography camera. A series of tests were made to investigate operating characteristics of the system. Figure 2.5 shows two ESPI images of a floppy disk obtained with two different system gain settings. Rendering was done with a Unix image processing utility. Results show that gain adjustments affect only the display of this system. They do not alter the numerical values stored in system output files. The only adjustment to pixel intensity is obtained by physical adjustment of the camera f-stop. Since optimization of shearograms calculated as the difference between ESPI's before and after loading requires recording of the ESPI's into the full dynamic range permitted by the data format, adjustment of the camera aperture is not a free measurement parameter. The camera f-stop should be chosen to stay just below saturation in the ESPI. Since the so-called "speckle diameter" is inversely proportional to aperture diameter, the requirement for near-saturation means that speckle diameter is fixed by illumination conditions. Therefore, speckle noise reduction (smoothing) must be addressed in data reduction, rather than by adjustment of camera settings.

Gain = 3.0   Gain = 4.5
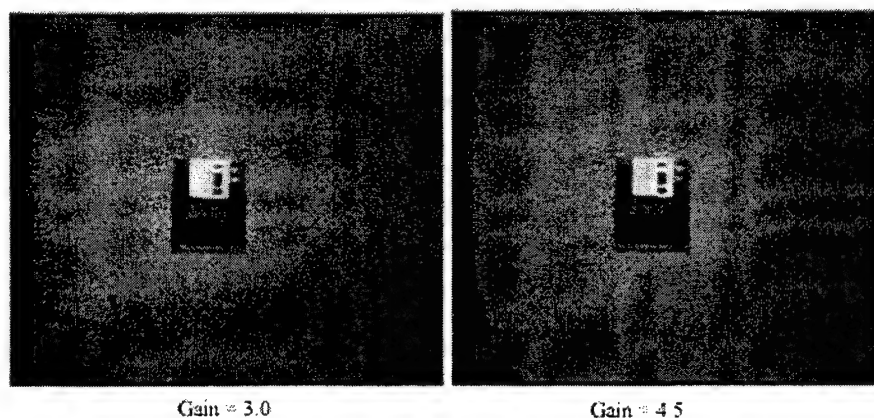
Figure 2.5.   LTI ES9150 Intensity calibration tests

Similarly, all other display controls were found to have no effect on the contents of the stored image files. The data represented by the file contents were found to be given by: 4*ABS(loaded image – unloaded image). Thus, the data files were determined to be rectified for this image processor. An older LTI ES-9150 image processor was found to truncate the output data.

2.4.3 Algorithm Performance

Normalized curvature image data, calculated as described, are load independent when displacement is linearly proportional to load. Initial tests verified this feature for pressure loading. Figure 2.6 illustrates this for synthetic shearograms produced by Cobra. Speckle is not included in these cases.
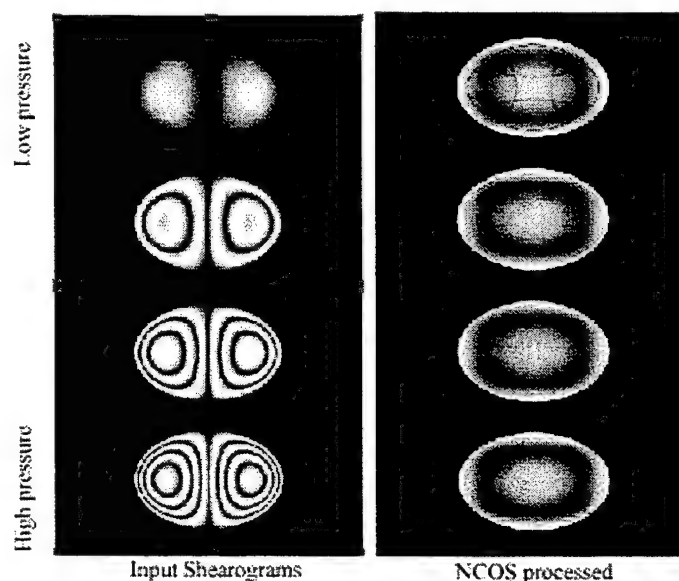
Figure 2.6. Normalized curvature images are load independent when displacement is linearly proportional to load

Normalizing curvature to peak value has the effect of normalizing load for those cases where displacement amplitude varies linearly with load intensity. This is rigorously the case for pressure loading, and for vibration, since the displacement function is multiplied by the load intensity. Even when the relationship between displacement is more complex, shearography requires such small displacements that load independence is a good approximation. Figure 2.6 shows raw x-shearograms for four different pressure loading conditions on the left. Normalized curvature, derived from these inputs is shown on the right. These results demonstrate that an output display, based on real-time evaluation of input shearograms will be an invariant, easily recognized pattern that eliminates ambiguity of interpretation for the operator.

13

2.5 Loading Models

The nature of various loading techniques was investigated for their application to shearography imaging. Three loading techniques were evaluated: vacuum loading, vibrational excitation, and thermal excitation. The first objective of theoretically evaluating loading methods was to guide optimization of loading techniques for particular types of structures. A second objective was to identify loading conditions under which the deformation detected by shearography can be maximally decoupled from general deformation of the structure. The theoretical deformation models were used to prepare input displacement models for the synthetic shearography code, Cobra.

Results of Cobra analysis were compared with experiments using the test phantom described above. Orthogonal shear images were acquired using vacuum, vibration and thermal loading.

2.5.1 Vacuum Excitation

Vacuum excitation is the most commonly chosen part excitation method, due primarily to its ease of application and simplicity of the associated equipment. However, this method is well suited for only a limited class of structures that will respond to a pressure differential (e.g., a composite honeycomb buildup which traps air internally). The technique is not suitable for stiff structures without any source-air that can expand to produce surface deformation when one surface is partially evacuated. The displacement function for a circular diaphragm, undergoing pressure or vacuum loading is given by:

$$ w = \frac{q}{64D} \left(a^2 - r^2 \right)^2 \qquad (7) $$

q = the uniformly distributed pressure differential

a = the radius of the diaphragm

r = the radial distance of any point of the diaphragm

$D = \dfrac{Eh^3}{12(1 - v^2)}$ = the flexural rigidity of the plate

h = diaphragm thickness

E = Young's modulus

v = Poisson's ratio

It can be seen from the equation that the deformation varies inversely with the diaphragm thickness, h, raised to the third power. Consequently, vacuum excitation works best for honeycomb structures in which the face sheets are very thin. One exception is inspection of silastic coatings, which have an extremely low modulus. Shearography fringe modulation

14

varies with the surface slope. Hence, fringe modulation varies with the square of a disbond diameter, "2a", making small disbonds difficult to excite.

2.5.2 Vibration Excitation

Vibration excitation is applicable to some structures for which vacuum loading is suitable (such as the debond phantom), and to an additional class of structures that cannot be excited by vacuum (such as those that do not trap gas). Thin metallic structures with plate-like geometries are good candidates for vibrational excitation. An example would be aircraft lap joints. The method is limited by practical bounds on driving frequencies since obtaining a detectable part response relies on operations at-or-near resonance conditions for the defects. Frequency sweeping is required to excite all possible defects at their corresponding fundamental frequencies. The experimental setup for vibration excited shearography is shown in Figure 2.7.
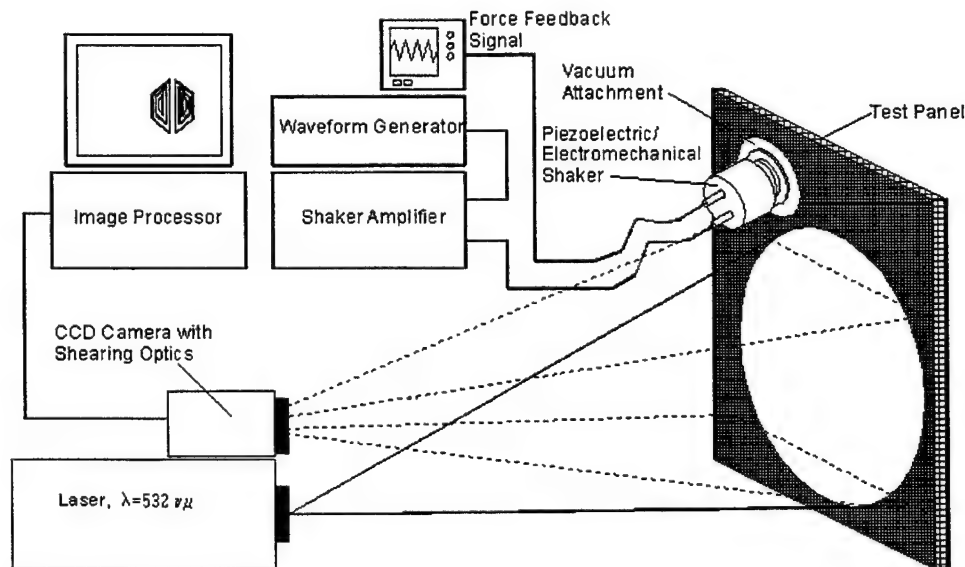
Figure 2.7. Experimental setup for vibrational excitation

The first configuration was based on a dual mode piezoelectric/electromechanical shaker with a forcing frequency range from 100 Hz to 65 kHz. The shaker was driven by a Wilcox Research PA7D Power Amplifier. A programmable function generator was used to perform an automated frequency sweep to ensure excitation of the natural frequencies of all the defects. For this testing, data were collected by manually adjusting the driving frequency as well as programmed sweeping. The dual mode shaker was attached at one corner of the test phantom using a vacuum attachment mount. Acoustic waves were then transmitted to the diaphragms through the aluminum structure.

Another approach was to acoustically excite the test phantom with a loud speaker. The frequency generator was used to drive the loud speaker to excite the diaphragms. This technique may be hazardous to the operator without combined earplugs and earmuffs.

Response modeling must address the problem of a forced harmonic excitation with damping. Solutions exist for undamped free vibration of a clamped circular plate using classical plate theory, but no solution was found for forced harmonic excitation of a plate with damping. In order to predict the response of realistic diaphragms, we took the practical approach of combining the forced response of a damped, single-degree-of-freedom (SDOF) system with mode shapes predicted by classical plate theory for a clamped circular plate. The resulting displacement equation is:

$$w(r,\theta,\omega,t) = m(\omega)W_n(r,\theta)\cos(\omega t) \qquad (8)$$

w = dynamic plate out-of-plane deformations

m = magnification factor from S.D.O.F. system

W_n = mode shape

$r,\ \theta$ = spatial coordinates

ω = forcing frequency

$$W_n(r,\theta) = A_n\left[J_n\left(\frac{\lambda_n r}{a}\right) - \frac{J_n(\lambda_n)}{I_n(\lambda_n)}I_n\left(\frac{\lambda_n r}{a}\right)\right]\cos(n\theta) \qquad (9)$$

A_n = Undetermined magnitude constant dependent upon experimental conditions that may be difficult to define

J_n = Bessel function

I_n = modified Bessel function

λ_n = Eigenvalue from classical plate theory solution

n = modal number

$$m(\omega) = \left. 1 \middle/ \sqrt{\left[1 - (\omega/\omega_n)^2\right]^2 + \left[2\xi(\omega/\omega_n)\right]^2} \right. \qquad (10)$$

ω = driving frequency

ω_n = natural frequency of mode

ξ damping ratio;   (Note that Q = $1/2\xi$ = $1/\eta$ where η=loss coefficient)
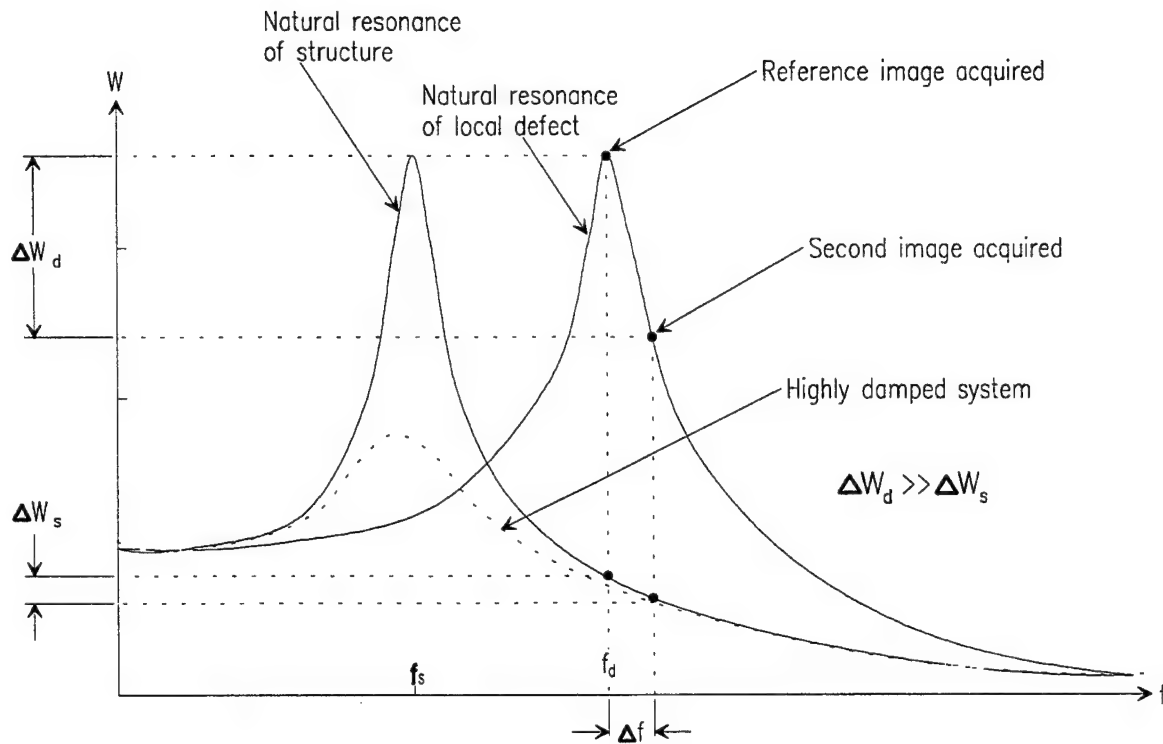
Figure 2.8.   Defect response relative to structure response for vibration excitation

Figure 2.8 qualitatively demonstrates the natural tendency of vibration excitation to separate the response of the defect from the normal harmonic response of the basic structure. The forced harmonic response of both the defect and structural response is modeled as a damped Single-Degree-Of-Freedom (S.D.O.F.) system. The natural frequency of the defect will tend to be much higher than that of the structure (based on size and mass). When the reference image is taken in the quiescent state, the maximum response of the defect occurs near the resonant frequency of the defect. At this same frequency, the response of the structure would be minimal. A similar effect occurs when the reference image is captured at the defect resonance and the disbond is clearly indicated by a slight detune in frequency without causing significant displacement changes in the structure. The model also predicts that lightly damped aluminum structures permit effective decoupling of the resonance response due to the sharpness of the resonance peak.

The general response model for vibration of the shearography phantom was taken to be the sum of each of the modal response predicted by Equation (8) up to the seventh mode of each diaphragm.

2.5.3 Thermal Excitation

Defect modeling for a heat flux from one side would be modeled by a clamped circular plate constrained by a rigid boundary and subjected to a transient temperature change. One would expect the one-sided heat flux to initially bulge the diaphragm towards the heat source due to thermal bending. As the temperature of the diaphragm increases, relative to the constraining

17

structure with high thermal mass, the diaphragm would expand at a greater rate than the surrounding structure. The constrained diaphragm would assume a buckled mode shape as the constraining structure applies a circumferential reaction force to the diaphragm. This buckling mode shape is the deformation detected by shearography.

A review of the literature did not reveal an appropriate model for the thermal buckling of the diaphragm. Theoretical development of such a solution was deemed beyond the scope of this study. Reismann[2] has developed the model for the buckling of a circular plate subjected to a uniform circumferential load. The surface deformation is in the form:

$$\frac{dw}{dr} = \phi = C_1 J_1(\alpha r) \qquad (11)$$

$$\alpha^2 = \frac{h\sigma_r}{D} \qquad (12)$$

J_1 = Bessel function

C_1 = Constant to be determined by the boundary conditions

h = plate thickness

D = flexural rigidity (previously defined)

σ_r = Uniformly distributed radial stress

The radial-circumferential stress is expected to vary directly with temperature change and the coefficient of thermal expansion. The buckled shape (after integration of ϕ), assumes the Bessel function shape, J_o, as was the case for the first mode of a vibrating diaphragm.

The advantage of thermal excitation is that certain structures, which cannot effectively be excited by vibration, or vacuum loading, may respond better to thermal loading. A significant practical disadvantage is that the heated surface tends to produce convection currents that cause significant spurious fringe noise in the image. This is mitigated, to some extent by flash heating.

2.6 Model Shearograms

Synthetic shearograms calculated from the displacement models above were used to test the NCOS algorithm developed under this task. The algorithm is incorporated in a developmental code "Shearp" which is a member of the Inders-code family developed at Boeing for NDE data interpretation. Two additional Boeing codes were developed for synthesizing shearograms (without speckle) for fast-turn-around tests of the algorithm. One, "Synthshear", calculates orthogonal shearograms for displacement distributions produced by pressure loading of uniform circular diaphragms. Results from this code, used during this task, were rectified, although capability for calculating unrectified shearograms was recently added. A second, "Makebs", calculates shearograms for complex, interacting distributions of

circular displacement fields representative of the damage pattern one might expect from a bird-strike. With this code, the displacement at each contributing damage site is described by a circular Gaussian function. Contributions from each site are summed. Shearograms are calculated from the local phase shifts resulting from displacement of the combined defects relative to an undeformed reference plane. The result is a complex shearogram, difficult to interpret directly. Makebs shearograms are unrectified. Sample results were shown in Figure 1.3.

Cobra, from Sandia, produces rectified shearograms with and without speckle. It accepts arbitrary displacement models in a variety of finite element file formats.

A description for the pressure loaded debond phantom was derived during this task and input to Cobra. This displacement function was assembled from the additive superposition of the vacuum loading displacement model described above, centered on each diaphragm, with the debond substrate rigid. Figure 2.9 shows Cobra calculated shearograms, with speckle, based on this input model. Shearing angles of 0.5 and 2.0 degrees are illustrated.

The figure illustrates an important consideration for shearogram acquisition. When the shearing angle is set to 0.5 degrees and the separation of the camera from the part is 48", classic butterfly patterns are produced from the circular debonds. The two lobes are closely spaced for the larger diaphragms, and a little less so for the smaller ones. In the former case, the footprint of the shearogram is nearly equal to that of the input displacement . When the shearing angle is increased by a factor of 4, the lobes become widely separated for all but the largest, most deformed diaphragms. The curvature image will extend over the footprint of the butterfly pattern, and will have a diameter equal to the actual diaphragm diameter plus twice the shearing offset $S*\alpha$. Thus, the defect localization will be relatively poor when S and/or α are large. The shearing angle should be chosen so that the shearing offset is a small fraction of the minimum defect diameter of interest, if good fidelity in defect localization is to be achieved. Unfortunately, reduction of the shearing angle is accompanied by a proportional reduction in shearogram sensitivity, as shown by equation (4). Thus, it is necessary to balance defect detectability against localization fidelity.

Shearing angle = 0.5 degree   Shearing angle = 2.0 degree
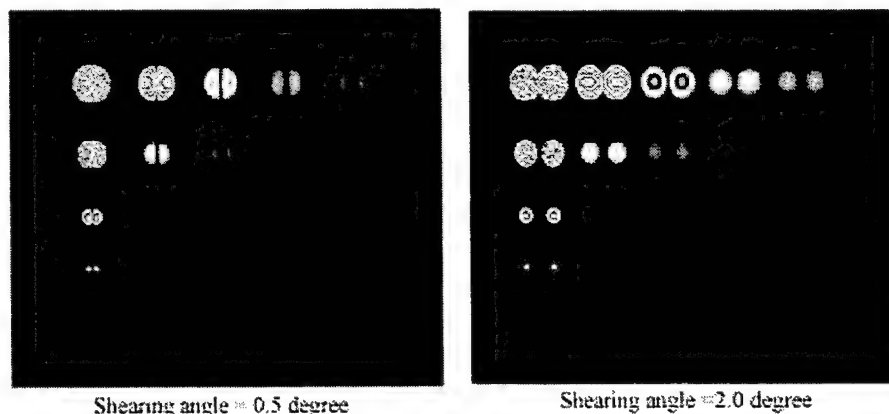
Figure 2.9.   Comparison of synthetic shearograms calculated with Cobra for the debond phantom for two values of shearing angle

A second displacement description was derived for vibrational excitation of the debond phantom using the frequency selective mode shape functions presented above. Damping in aluminum is relatively weak so the modes are observed over a small frequency range, and will only be detected if a swept frequency generator is used. Composites are more strongly damped so that a response will be observed over a larger frequency interval, although the maximum amplitude will be reduced relative to a less damped material. The Cobra input displacement file entry for each defect is the superposition of available modes up to the seventh order. Because of the frequency selection, one mode dominates with small contributions from others in some cases. Software switches were included in the displacement generator to facilitate selection of any one of the available modes at each diaphragm. It was also possible to turn off frequency selection so that all diaphragm mode shapes could be represented simultaneously. Much of the processing algorithm development work was done with additional, synthetic coupons featuring only one defect. These were typically 3" square with a centered diaphragm, using the same defect models discussed above, to facilitate rapid turn around for NCOS algorithm development and trouble shooting.

Figure 2.10 shows a Cobra shearogram for a 3" coupon with a 1.5" diameter, 0.01" thick diaphragm for a fundamental mode (a), and for a first order mode (b). The calculated response frequency for the fundamental mode was 1.75 kHz, which agrees well with observations on the debond phantom. The fundamental mode shearogram, shown as Figure 2.10 (c) was taken from the phantom diaphragm having the dimensions above.

(a)   (b)   (c)
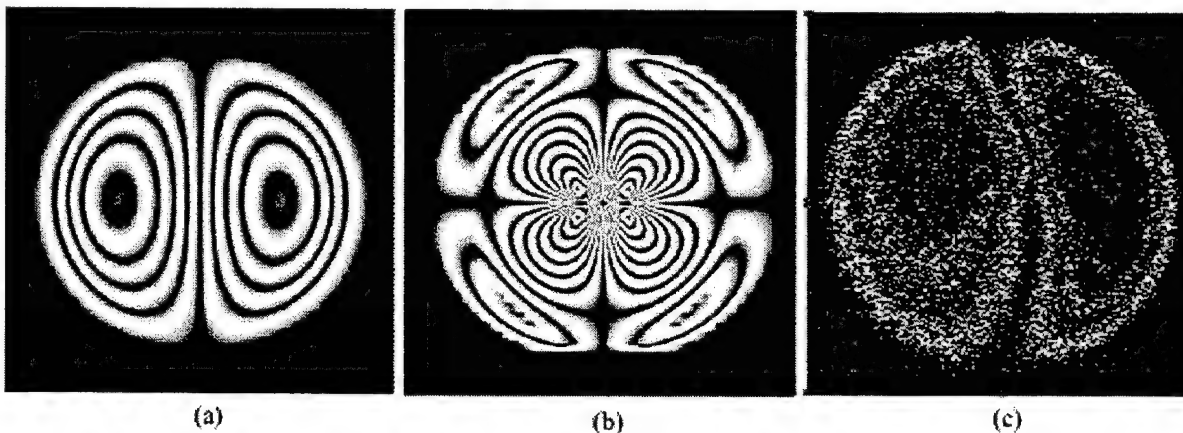
Figure 2.10.   Cobra shearograms for the fundamental mode (a), and first order (b) mode response of 1.5" diameter, 0.01" thick diaphragms. A measured shearogram from the same diaphragm on the debond phantom is also shown (c).

The correspondence between predicted frequencies and measured response frequencies was extensively characterized. The results, which show very close agreement, are given in Table 2.1.

Table 2.1. Comparison of predicted and measured diapragm mode frequencies for the debond phantom.

| Dia inches	Thick inches	Mode Indices	F-kHz Theo.	F-kHz Exp.	Ratio	% Error
2.00	0.01	0,0	0.987	0.966	1.022	2.2%
2.00	0.01	1,0	2.054	1.926	1.066	6.6%
2.00	0.01	2,0	3.369	3.18	1.059	5.9%
2.00	0.01	0,1	3.842	4.04	0.951	-4.9%
2.00	0.01	3,0	4.93	4.9	1.006	0.6%
2.00	0.03	0,0	2.962	2.8	1.058	5.8%
2.00	0.03	1,0	6.161	5.94	1.037	3.7%
2.00	0.03	2,0	10.108	9.82	1.029	2.9%
2.00	0.03	0,1	11.52	11.25	1.024	2.4%
2.00	0.03	3,0	14.791	14.42	1.026	2.6%
2.00	0.05	0,0	4.936	4.79	1.030	3.0%
2.00	0.05	1,0	10.268	9.82	1.046	4.6%
2.00	0.05	2,0	16.847			
2.00	0.05	0,1	19.209			
2.00	0.05	3,0	24.652			
1.50	0.01	0,0	1.755	1.754	1.001	0.1%
1.50	0.01	1,0	3.651	3.57	1.023	2.3%
1.50	0.01	2,0	5.99	5.95	1.007	0.7%
1.50	0.01	0,1	6.83	7.18	0.951	-4.9%
1.50	0.01	3,0	8.765	8.68	1.010	1.0%
1.50	0.03	0,0	5.265	5.03	1.047	4.7%
1.50	0.03	1,0	10.953	10.54	1.039	3.9%
1.50	0.03	2,0	17.97			
1.50	0.03	0,1	20.489			
1.50	0.05	0,0	8.775	8.22	1.068	6.8%
1.50	0.05	1,0	18.255			
1.00	0.01	0,0	3.949	3.73	1.059	5.9%
1.00	0.01	1,0	8.215	8.31	0.989	-1.1%
1.00	0.03	0,0	11.847	11.25	1.053	5.3%
1.00	0.03	1,0	24.644			

Measurements were made using a contact, dual element shaker, which combines an electromagnetic driver, and piezoelectric element. It was used to deliver required power over a range from about 100 Hz to 10 kHz in these response characterization tests. Part contact was made in one corner of the phantom. Excitation of individual diaphragms relied on acoustic wave propagation to the site. A loud speaker was also used to air-couple acoustic energy to the part up to about 15 kHz during frequency response characterization. In both instances, it is difficult to predict the driving function at the diaphragm location.

Cobra calculates shearograms, with and without speckle for specified loading conditions. If vibrational excitation is chosen, Cobra averages the dynamic image-plane data over time, since the camera frame-rate is generally slower than the oscillation frequency of the excited

defect. The result is a sum of views obtained at intervals corresponding to the inverse of the camera frame rate (e.g., 33 msec/frame), minus an increment for data storage. This sum is equivalent to the difference between a tare shot and a loaded shot, so that it is not required that a tare image be subtracted when using vibration (although it is commonly done). If a tare image is subtracted, it is common to acquire it with the shaker on, but tuned off resonance to minimize contributions from rigid body motion as discussed in Section 2.5.2. The shearogram represents integration of the displacement function for the vibrational case over the observation (frame) time. The resulting fringe distribution is given by the zeroth order Bessel function of the product of an instrument constant, times the displacement gradient. Unfortunately, there is no analytic expression for the spatial derivative of the inverse of a zeroth order Bessel function (as there was with the arcsine function encountered for static loading conditions). Therefore, interpretation of data obtained with vibrational excitation is less straightforward than the cases of vacuum/pressure, and thermal loading. This is discussed further in subsequent sections.

2.7 Results

The NCOS algorithm was tested using both synthetic, and real shearograms. All commercial instrumentation tested produced rectified, or truncated data files. To produce simple subtractions of contributing ESPI's appropriate subtraction algorithms were applied to input ESPI image data obtained from shearographic cameras, or from synthetic shearogram inputs, without speckle.

2.7.1 Development using Cobra

The commercial shearography systems tested, all employed 8-bit resolution for ESPI acquisition. Shearograms calculated from the stored images had reduced resolution since they represent the pixel-by-pixel difference between two eight bit images where the subtracted values generally differ from one another by a small amount. The resultant shearograms are estimated to exhibit only 3-to-4 bits dynamic range. In addition, the fringes are embedded in a speckle field, making the data effectively quite noisy. Development of data processing algorithms, based on measured data of this type is made more complicated because issues of low dynamic range and data smoothing must be addressed simultaneously with basic issues of fringe interpretation.

Cobra, therefore, provided an excellent tool for development. The data have a high dynamic range, and shearograms can be produced with, or without speckle. The first clear indications of problems with processing rectified data were observed with Cobra. Attempts to calculate curvature images from Cobra shearograms consistently resulted in high/low ambiguities in the grayscale representation. This result was obtained with, and without speckle, and could not be traced to problems with number representation in the NCOS algorithm or in the viewers used to evaluate the curvature images. Various combinations of summing non-absolute and absolute values of the second partial derivatives calculated from data did not resolve the problem which is illustrated in Figure 2.11. The figure also includes an example of a curvature image calculated from the displacement field from which the shearograms were derived. The latter correctly shows maximum curvature only at the edge of the diaphragm as expected.

22

Curvature from rectified input   Curvature from displacement
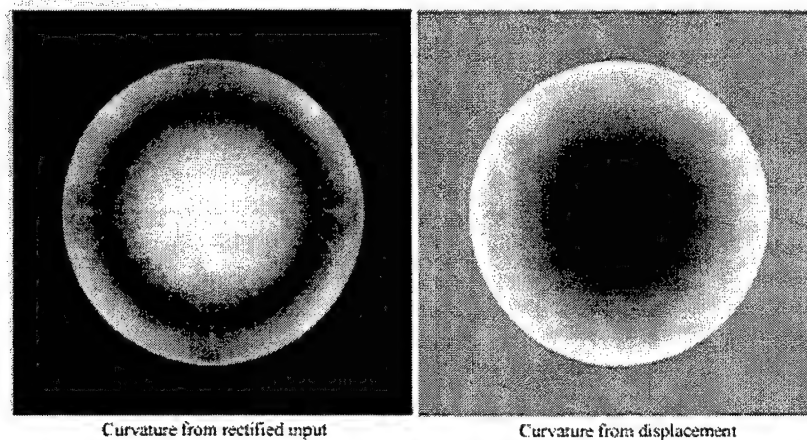
Figure 2.11.   Curvature images calculated from rectified synthetic shearograms illustrating high/low grayscale ambiguity. Results are compared with a curvature image calculated from the input displacement function.

Shearogram registration.   Feature extraction assumes registration of the x- and y-shearograms. This will not, in general, be true. A shearing camera, equipped with a simple wedge over half the entrance pupil will offset the apparent position of the part by half of the shearing distance in the direction of shear.   Therefore, the x- and y-shearograms are inherently misregistered and must be corrected.   This is not always the case.   LTI uses shearing optics that displaces the two sheared images equally and oppositely to one another to minimize misregistration. However, the shearing element must be rotated to produce the two orthogonal cases, and misregistration can occur as a result of inexact mounting of the element, for example.

Cobra shearograms are produced with image misregistration. Modifications were made to NCOS to provide for an offset in the two orthogonal shearograms to correct for this. The result, which presently requires operator interaction, is illustrated in Figure 2.12.

(a)   (b)
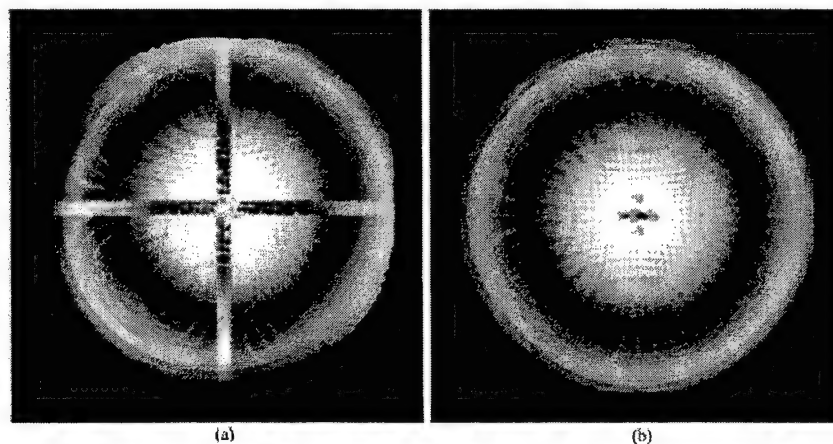
Figure 2.12.   Processed Cobra shearograms illustrating registration of the two contributions: (a) raw, unregistered shearograms used; (b) after registration by 14 pixel shift in x- and y axes

23

The figure shows results of processing Cobra (rectified) shearograms without first shifting one with respect to the other to register them. There is a 14 pixel offset of the apparent position of the flaw in both axes that accounts for the cross pattern in the NCOS processed data (Figure 2.12(a)). There is also some fineline "decoration" in the figure background that is skewed. Figure 2.12(b) shows the outcome in the processed data when a 14 pixel shift is introduced in both axes.

The cross disappears, and the background decoration also becomes symmetric, indicating the correctness of the offset correction. The decoration occurs because the algorithm yields artifacts (that can be filtered) when arcsine is $\pm\pi/2$. Automation of this process was not addressed during this effort, but the registration procedure is general, and can be applied to any shearogram pair. Practical implementation requires that data be obtained from a symmetric feature, such as a circular diaphragm, as part of a calibration procedure, to determine the required offset values for any system.

Speckle smoothing. Speckle shearograms exist because of the presence of speckle, which has a modulation equal to the maximum modulation of the fringes. Elimination of speckle would also eliminate the fringes. However, speckle smoothing can be done, to improve fringe recognition. The desirability of this is illustrated in Figure 2.13, which shows, (a), an intensity profile through a Cobra shearogram, without speckle, calculated for a statically loaded diaphragm. The intensity profile is shown for the left side of the symmetric pattern, and is calculated along a single row of image pixels on the vertical centerline. The figure also shows a similar intensity profile, (b), for a Cobra shearogram with speckle to illustrate the modulation function underlying the speckle image. This figure compares the intensity profile for one row of centerline pixels with that obtained by averaging over nine pixels about center. While not as well defined as the intensity profile of (a), the sinusoidal modulation is more clearly evident with averaging. Figure 2.13(c) shows an intensity profile below center without speckle, and Figure 2.13 (d) is similar to (b) for this off center case. This figure illustrates an approach to speckle-noise reduction, using simple averaging, that enhances fringe recognition. More advanced smoothing methods were introduced into the NCOS algorithm, as illustrated below.

(a) Intensity profile for left half of pattern with no speckle

(b) Same with speckle. Averaging of 9 adjacent pixel rows is compared with single row profile

(c) No speckle, sampled below center

(d) 9-row averaging vs. 1 row for case (c) with speckle
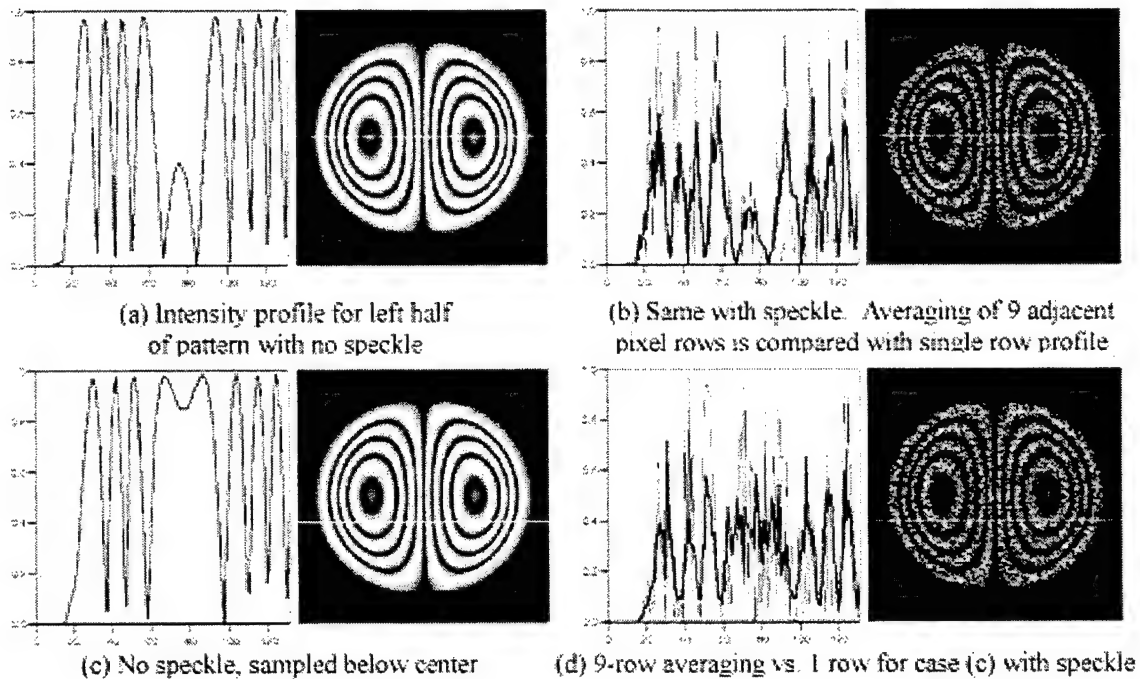
Figure 2.13. Improving fringe interpretation in speckle interferograms

Calculation of curvature when vibrational excitation is used. Figure 2.14 shows intensity profiles from Cobra shearograms before and after speckle was added. for the vibrational excitation case. As can be seen in 2.14(a), which has no speckle and isolates the basic fringe modulation, oscillations are not bounded by ± 1 because the fringes are described by the zeroth order Bessel function of an argument that is proportional to surface gradient in the shearing direction. Figure 2.14(b) shows the effect of speckle on the intensity profile, and also illustrates the result of 9-row averaging for speckle reduction (as in 2.13 (b)). Figure 2.14(c) shows the result of boxcar averaging on speckle reduction. This more sophisticated filtering routine averages speckle over the neighborhood of each pixel. These results were obtained for a particular trial filter, and are not necessarily optimized for the speckle size of the input shearogram. Further development and optimization of filtering techniques should be undertaken as part of a system development effort.

25

(a) Cobra vibrational shearogram without speckle

(b) Case with speckle comparing 9-row average with 1-row profile for speckle smoothing

(c) Use of boxcar averaging for speckle smoothing
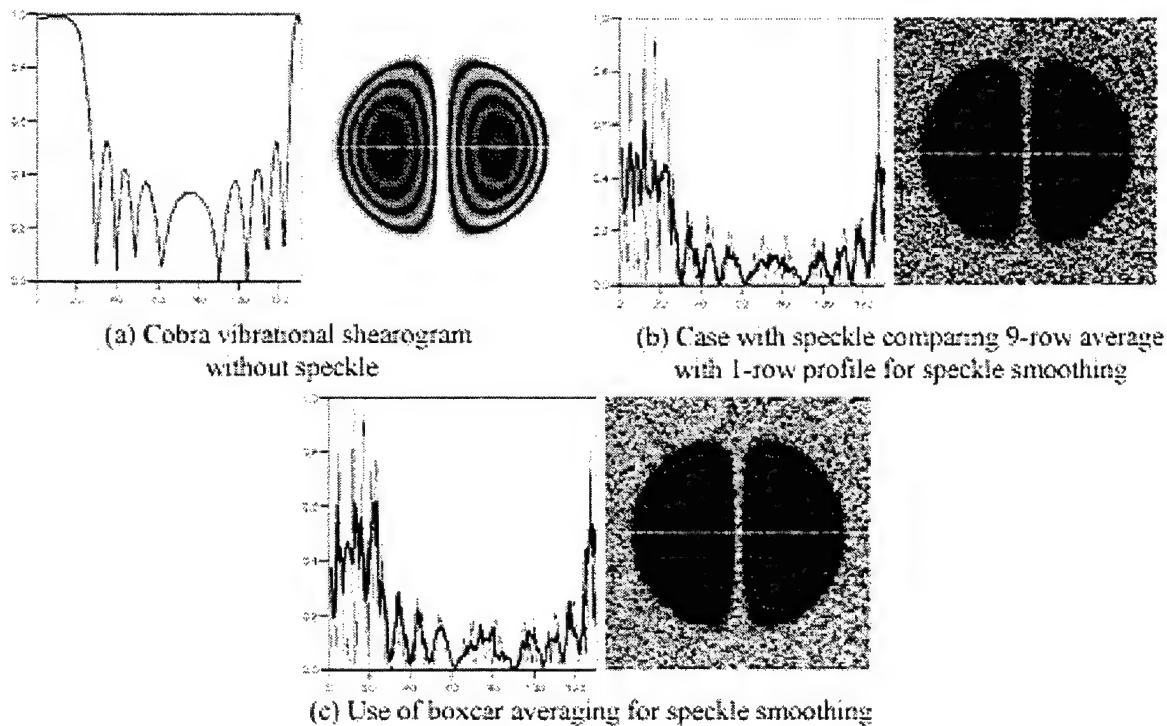
Figure 2.14. Illustration of fringe modulation when vibrational excitation is used. (a) without speckle (b) 9-row average to smooth speckle; (c) boxcar averaging to smooth speckle

For static loading, where the fringes are sine-modulated, use of an analytical form for the derivative of the arcsine facilitated calculation of the Laplacian because it obviated the need to resolve the principal value ambiguity. A principal value ambiguity also exists, for Bessel function modulated fringes, but no analytic expression for the derivative of the inverse Bessel function is known. This problem was not resolved. Given the limited dynamic range of the shearograms obtained with available equipment, there appears to be little loss of fidelity when vibrational shearograms are reduced as if the fringes were sine modulated. This is illustrated in Figure 2.15 which compares the results of NCOS processing of a Cobra shearogram-pair calculated for vibrational loading, with the curvature calculated from the same input mode shape without vibration. The gray scale ambiguity discussed above is present because Cobra has not yet been upgraded for calculation of unrectified shearograms. Deriving an improved algorithm for feature extraction in the vibrational case should be addressed as part of an equipment upgrade program.
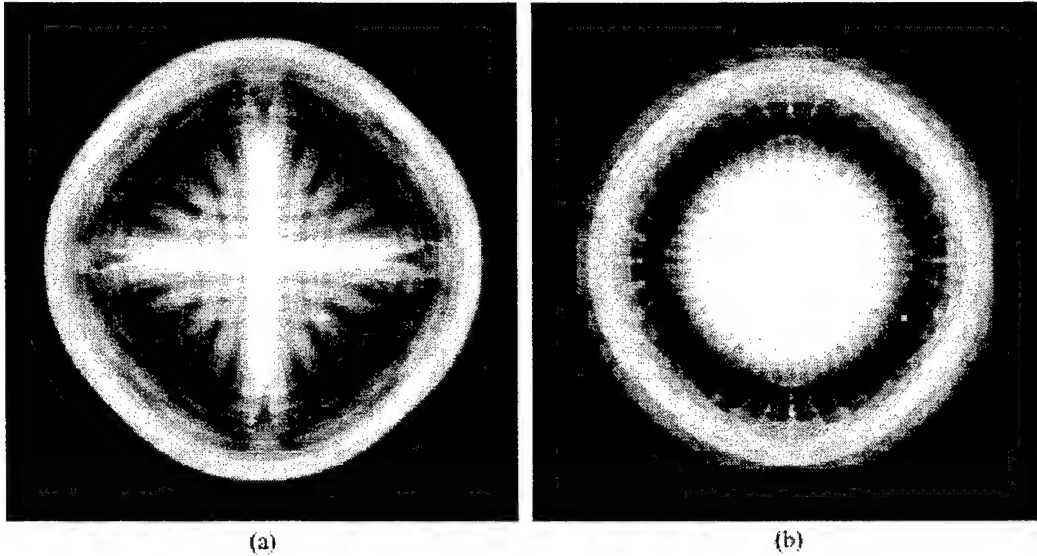
Figure 2.15.   Comparison of NCOS processed, Cobra -shearograms obtained from the vibration input mode function, with vibration turned on (a) and off (b)

2.7.2 Development using "Bird Strike"

Figure 1.3 showed a synthetic, unrectified shearogram generated by the code "makebs". The image results from the additive combination of overlapping displacement functions representing the kind of damage one might expect from a bird strike. The displacement functions are Gaussian, which is a simplified representation of real debonds, but they provide an easily synthesized distribution yielding a useful case for development.

Figure 2.16 (a) and (b) shows the two input shearograms, along with curvature calculated from the input displacement function (Figure 2.16(c)). Curvature calculated from the NCOS algorithm is shown as (d). Agreement between the directly calculated curvature and the processed shearograms is excellent in this case. It is important to note that the processing effectively localized damage sites. This ability to localize damage sites from rather diffuse input shearograms provides an excellent tool for evaluating whether repair is needed in areas where damage has been found.
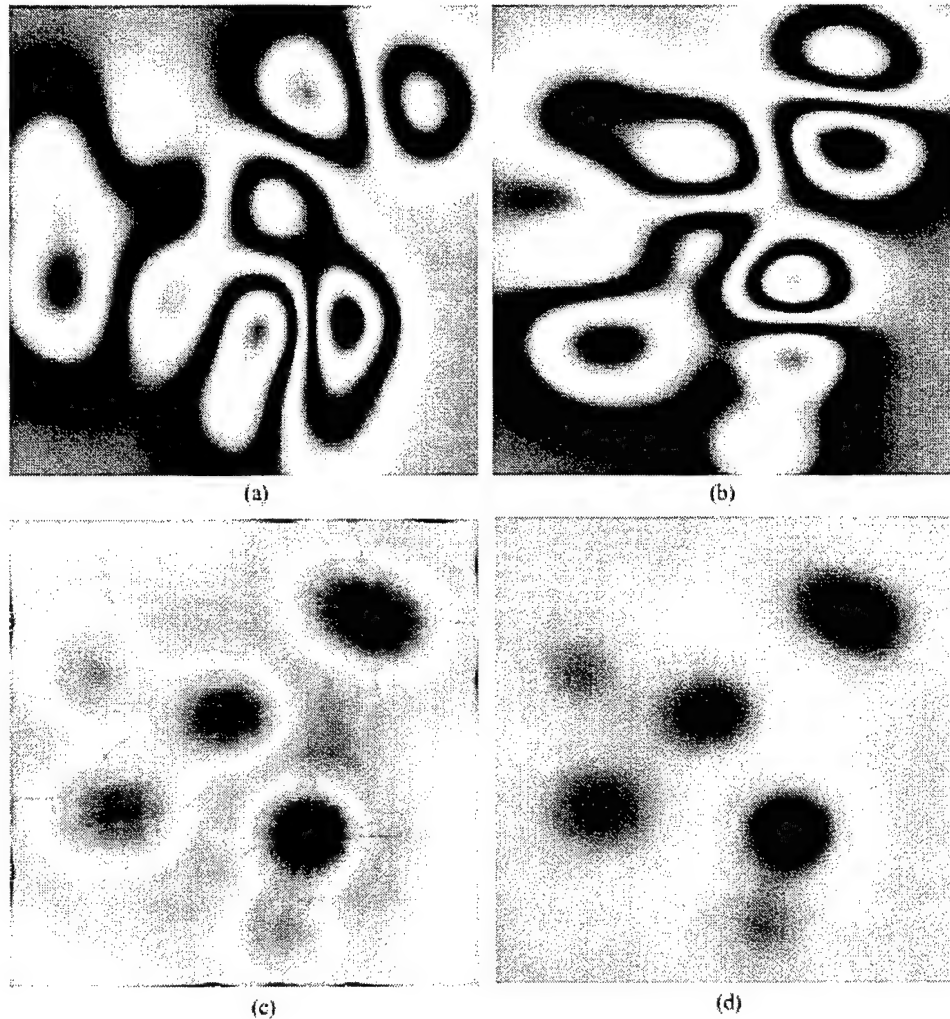
Figure 2.16.   Comparison of processed curvature with curvature from the input
displacement function for the "Bird Strike" shearograms

The results demonstrate the effectiveness of NCOS algorithm processing on unrectified shearograms, particularly when speckle is not present. Inclusion of speckle will degrade signal-to-noise, but should not prevent correct mapping of curvature. Smoothing and equalization of images derived from speckle shearograms will highlight and localize defects as illustrated here.

2.7.3 Evaluation of measured data

Composite Debond Phantom. Boeing has produced a number of debond phantoms that have been widely used in the NDE community to evaluate NDE methods for debond detection in composite assemblies. Figure 2.17 shows a schematic of one of the phantoms used in this program to indicate the position of inserts between plies for correlation with shearographic data presented in Figure 2.18. Note that inserts are located at multiple levels in the composite layup to simulate debonds at different ply locations. In particular, some are on the bottom side of the core. Figure 2.18 shows a shearogram obtained from this phantom using

vacuum loading in a Boeing-owned LTI ES-9150 system. It is compared with a NCOS curvature image that clearly isolates debonds at multiple levels of the phantom. Although the input shearograms were rectified, use of smoothing and image intensity distribution equalization on the calculated curvature image enhances detection of the defects in this phantom.
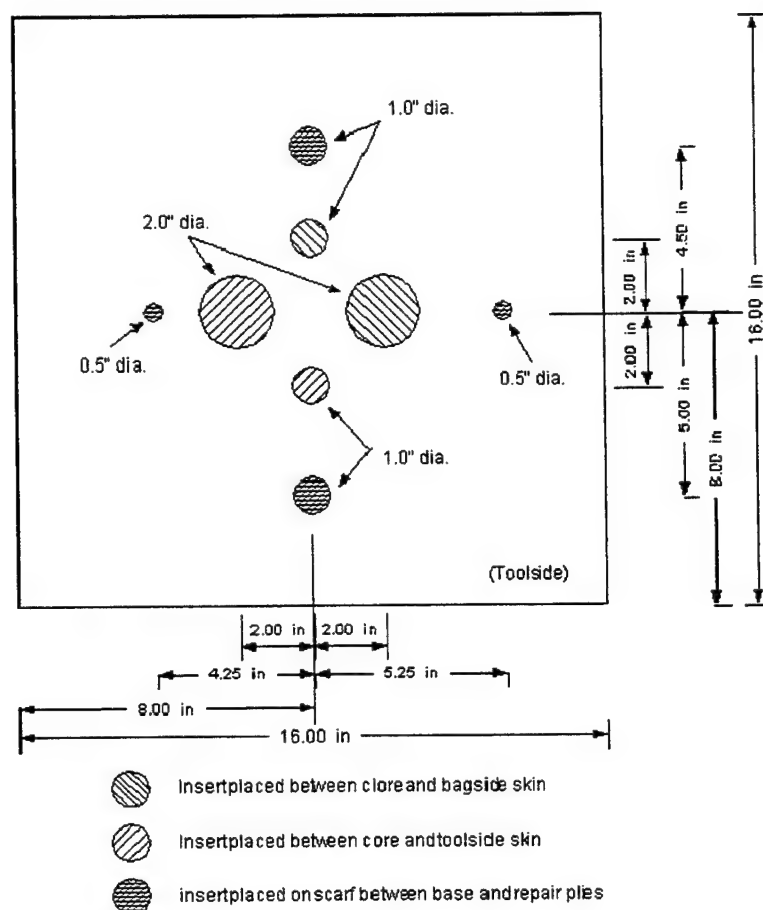

Figure 2.17.   Schematic of Boeing-built composite debond phantom

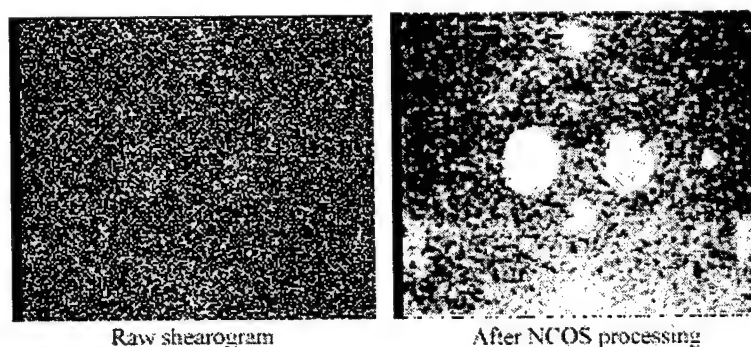Raw shearogram   After NCOS processing

Figure 2.18.   Shearogram from vacuum loaded composite debond phantom compared to its processed curvature image

Composite Spoiler. Figure 2.19 shows a photograph of a composite spoiler panel with elongated, parallel debonds. The debond areas were outlined with an indelible marker, and can be seen in the photograph.
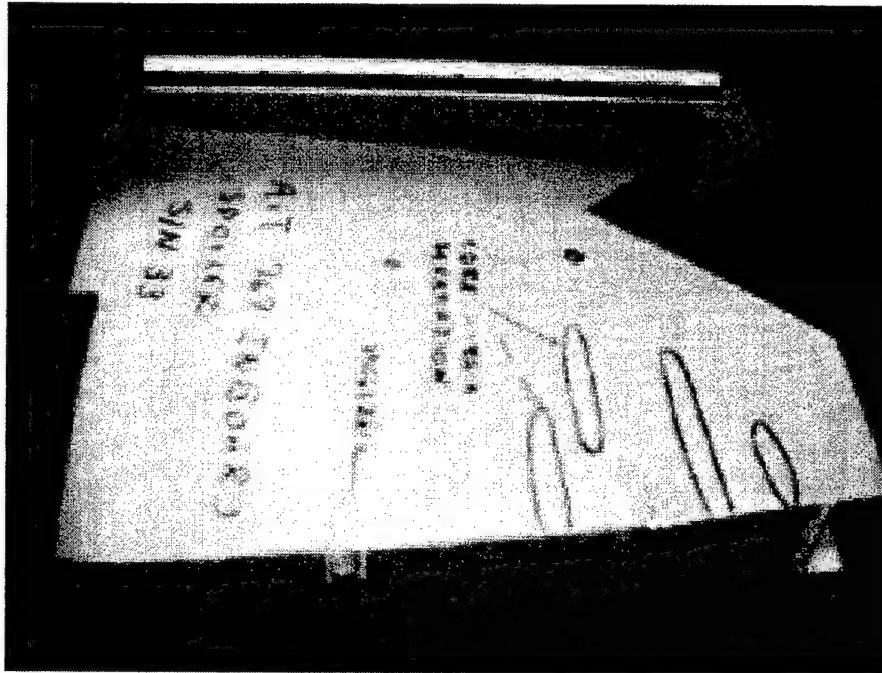
Figure 2.19.   Photograph of spoiler panel showing debond locations

Figure 2.20 (a) and (b) show respectively, the unloaded ESPI and the loaded ESPI when the panel was vacuum loaded at 1.2 psi using the LTI ES-9150 vacuum loading system. The camera setback from the part was 30", and the shearing angle was 0.5 degrees. Figure 2.20(c) and (d) are unrectified shearograms calculated from appropriate x- and y ESPI's. Note that the fringe contrast is very poor in these images because the zeros of the fringe modulation occur at the mid-range of the gray-scale and are therefore gray, not black. This is the principal reason for rectification of shearograms when operator viewing is required. Rectification makes the modulation zeroes minimum values, and therefore black when displayed. Examples of rectified shearograms are shown at the bottom of the figure (f) and (g). The result of NCOS processing of the unrectified shearograms is shown in figure 2.20(e).

The known debonds are localized and enhanced by the processing. Note that the upper right debond is larger than sketched by an operator prior to test. The central, lower debond appears to be stiff, and perhaps less thoroughly debonded than the sketch suggests. The left debond appears to correspond to the originally estimated size. The processed data have a very limited dynamic range, and may not have optimum speckle noise reduction. These are areas in which continued development of the data acquisition and processing will be required.

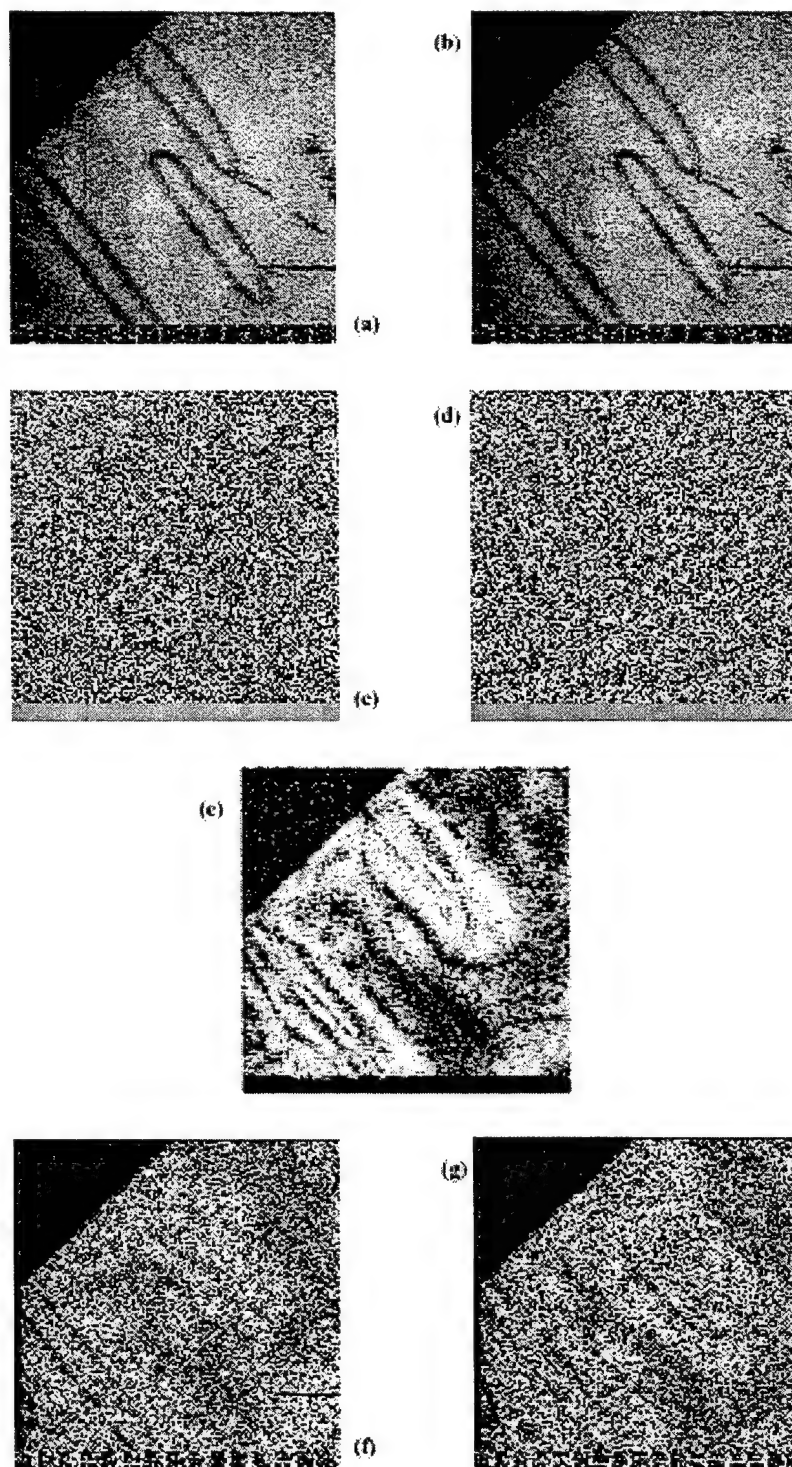Figure 2.20. (a) Unloaded x-ESPI; (b) loaded x-ESPI; (c) unrectified x- and (d) y-shearograms; (e) calculated curvature; (f) x-rectified and (g) y-rectified shearograms from vacuum loaded spoiler panel

31

2.7.4 Considerations for Experimental Implementation

This section covers practical implementation of a fieldable system that incorporates ideas discussed above. This method relies on acquisition of two, co-registered orthogonal shearograms. When loading is static (e.g., pressure/vacuum), or steady state (e.g., vibrational at constant frequency), it is possible to acquire two shearograms at arbitrary times. When loading is transient, as it is for thermal, the two shearograms must be acquired under nominally the same conditions. This requires that they be recorded within no more than about 10% of the relaxation time of the temperature distribution (and preferably with considerably less delay). A measurement system that satisfies the conditions imposed by thermal loading will satisfy all requirements for pressure/vacuum, and vibrational loading.

In order to obtain data with thermal loading for this work, two LTI SC4000 cameras were mounted on a common optical table, each receiving an orthogonal image relative to the other. The two cameras viewed the part through a 50% beam splitter. Since the splitter provided both a view of the part and an alternative view from its other leg, it was necessary to place an absorbing beam stop so only the shearograms were recorded. Because the camera system was intended for use with radiant heat sources, in some instances, narrow band filters centered on the illuminating laser wavelength were also incorporated to prevent camera overload during the heating cycle.

The optical axes of the two cameras were co-aligned with as high an accuracy as could be achieved with the non-precision mounting. Any residual misalignment could then be compensated for in software. This included compensation for optical defects such as pincushion distortion, and astigmatism. Since the beam splitter produced a mirror reversal in the reflected optical path, the transformation also had to reverse the image from the reflected leg of the beam splitter. These distortions were identified and corrected for by calculation of a polynomial transformation function derived so as to register fiducials in measured calibration images. This transformation function could then be applied to all data reduction from the two-camera system.

Several thermal excitation systems were evaluated. Use of a heat gun was eliminated immediately based on past experience. Forced convection leaves large scale motion in the heated air, long after the heat source is removed. Shadows of the convecting air are superimposed on the shearographic fringes, complicating interpretation.

Two radiant heat sources were found to be effective when used on the aluminum debond phantom. The first one tried was a high intensity photographic flash unit which easily produced multiple fringes from all diaphragms, although not simultaneously (i.e., excitation of the stiffer diaphragms required heat input that over-excited less stiff ones). The energy of the flash must be chosen for optimum excitation of each diaphragm based on its relative stiffness. Surprisingly, the flash system was not the best choice for thermal excitation in these experiments. The reason was that the two-cameras could not be triggered simultaneously because they shared a frame grabber. It was necessary to capture a shearogram from one camera and save it to memory before a second shearogram from the other camera could be recorded. The minimum time lag in this process was about 0.4

seconds. While flash heating deposited nearly uniform energy into diaphragms, the rate of change of temperature was high and redistribution of heat from the diaphragms to the more massive surrounding plate was rapid. Too much change occurred in 0.4 seconds for the two shearograms to approximate the same thermal strain state.

The second source tried was a standard hardware store heat lamp, mounted in a stationary position slightly behind the shearing camera. The phantom was heated for several seconds with the lamp, which was then turned off. This longer exposure apparently established a quasi-steady state heat flow so that the shearograms evolved less in the 0.4 second delay time, and the two interference patterns were nearly identical (except for orthogonal orientation). Initial expectations that a relatively extended heating cycle would result in convective plumes were not realized.

The camera separation from the phantom was 40 inches in these tests. The lens was zoomed so a single diaphragm could be examined at high magnification.

A practical system for field use could easily incorporate two cameras in the dual beam configuration used in the laboratory. Since CCD cameras are very compact and light-weight, a dual camera system would be nearly as compact and light weight as single beam cameras now in use.

Dual frame grabbers should be used to facilitate simultaneous acquisition of two orthogonal shearograms. Under these circumstances, the flash heat source should be preferred. It will permit near instantaneous heating, and if an extended heating cycle is required in some instances, multiple flashes could be employed. A flash source will generally be most effective in minimizing convection problems. It is also a good choice for simultaneously collecting multi-mode, complimentary shearograhy and thermography for data fusion.

A major deficiency of existing shearing camera systems is the use of 8-bit digitization, which results in low dynamic range shearograms. Ten bit (and possibly 12-bit) digitizers can be acquired with adequate speed to support a standard video frame rate and high resolution cameras. Their use would provide high fringe resolution, and a significant improvement in the fidelity of the input data used for curvature calculation in this method. Data must be acquired in an unrectified format.

Dedicated processors for data reduction should be incorporated so that real time curvature images can be computed and displayed for the operator, thus presenting shearographic data in an easily understood format, generally independent of specific loading conditions.

3.0   CONCLUSIONS

A feature extraction methodology was developed that is applicable to real-time display of processed images derived from speckle shearograms. The processed images show local, normalized curvature and greatly reduce the present ambiguity of interpretation associated with the raw input images. The method, which relies on computation of normalized curvature by appropriate differentiation of information encoded in orthogonal shearograms, is not affected by part orientation, or the viewing aspect of the shearing camera. The only effect of off-normal viewing is apparent perspective distortion familiar in normal vision.

The computational method was developed and refined with the aid of predictive displacement models for several loading methods applied to a debond phantom fabricated for this program. The phantom, which consisted of a thick aluminum plate with an array of thin, machined diaphragms represented typical aerospace structures with debonds. The displacement models were used in several predictive shearography codes, principally Cobra, from Sandia National Laboratories, as inputs for calculation of synthetic shearograms. Cobra is capable of producing synthetic shearograms with- and without speckle for a variety of loading conditions, (including vibration), and for complex geometries. Experimental shearograms were also obtained for vacuum/pressure, vibrational, and thermal loading conditions using the debond phantom and a variety of more complex parts.

Development of a feature extraction algorithm "NCOS" was successfully completed for cases where shearographic fringes are modulated by the sine function whose argument depends on the derivative of displacement along the shearing axis. The developed algorithm is suitable for implementation in a real-time viewing system that can provide a shearography technician a relatively unambiguous image of local surface curvature rather than the often confusing and difficult to interpret raw shearogram.

A baseline, two-camera measurement geometry was tested for simultaneous acquisition of orthogonal shearograms. Lessons learned from the use of this system provide the basis for implementation of a compact, fieldable system taking advantage of the feature extraction methods developed. A number of deficiencies in currently available shearographic instruments were identified as a result of this work. Chief among these are the use of 8-bit digitization for ESPI, which leads to very low dynamic range (i.e., 3 bit) in shearographic images, and the practice of rectifying shearographic data which aliases the calculation of surface curvature.

Three loading methods were investigated, analytically and/or experimentally, and their general range of applicability was identified. Vacuum/pressure loading was most generally useful in those cases where a source of trapped gas is available (such as for honeycomb composites). Implementation is simple, requiring only a pressure/vacuum fixture or a pressure/vacuum enclosure for the part. A pressure/vacuum fixture will not be applicable in the case of highly curved surfaces or complex shapes. Vibrational loading is effective for many of the same samples for which pressure/vacuum is applicable. This technique allows for interrogation of a wide range of defects, having resonances in the interval from about 100 Hz to 65 kHz when a swept frequency source such as a mechanical shaker, or a speaker is

34

employed. One drawback to vibrational excitation is that large amplitudes are required which necessitates protection for the operator as well as all other personnel in the test area. The preferred range of applicability for thermal loading has not been well characterized. Excellent response was achieved with the shearography phantom on which most diaphragms were easily excited. Thermal measurements were less encouraging on composites with realistic debonds. More analytical and experimental testing will be required to fully quantify this loading method.

Several items could not be resolved during this work. While predictive displacement models were developed for pressure/vacuum, and vibrational loading, a solution for displacement with thermal loading was not developed. Also, the fringe modulation uses the zeroth order Bessel function when vibrational loading is employed. A satisfactory method for demodulation of fringes of this type was not developed. However, use of the NCOS sine function decoding produces satisfactory results with the low dynamic range shearograms currently available.

The accomplishments of this program make it possible to transition shearography from a subjective inspection method with which it is difficult to identify and localize defects, to one that produces unambiguous defect indications with excellent localization. This is a critical step towards generation of a Technical Order for routine shearographic inspections at Government maintenance depots.

4.0 RECOMMENDATIONS

The work accomplished under this task has demonstrated the efficacy of NCOS curvature computation from orthogonal shearograms as a means of presenting an easily interpreted display to an inspector. If this methodology is to be moved from the laboratory to field implementation, some additional development is needed.

One candidate geometry for a fieldable system was tested during this work. It relies on use of two optically aligned shearing cameras, simultaneously recording the same scene through a beam splitter. Other designs can be postulated. The developmental system shared a frame grabber that prevented simultaneous image acquisition. One result was that flash lamp heating could not be demonstrated effectively for thermal loading, as discussed above. The probable superiority of flash heating can only be properly evaluated with a system that can acquire shearograms simultaneously.

Shearing systems available for these measurements had 8-bit resolution for ESPI's. This results in about 3-4 bit resolution in subtracted data. Low dynamic range is a present limitation on full implementation of this feature extraction method.

We recommend development of a brass board system to evaluate concepts for field implementation of curvature image calculation. This will include: (1) completion of a design study to select the best implementation geometry (e.g. the dual camera system tested during this task, or a single camera system using polarization to separate orthogonal images); (2) identification of a high-speed digitizer with 10- or higher-bit resolution; (3) selection of a high resolution camera, and: (4) trade off of resolution and digital depth (if required). In addition, a real-time processing and display system will be designed.

Following design selection, a prototype system will be built followed by testing with phantoms such as the one developed for this task, and realistic parts representing actual test problems. Tests should include the three loading methods evaluated during this task.

Unresolved issues from this task will be resolved. This will include optimizing data processing to minimize speckle noise, and upgrading feature extraction to process Bessel function modulated data. Modeling of thermally induced displacement will also be completed.

The result will be recommendations for a final design of a fieldable system, suitable for production by an established vendor, and guidelines for field use of the developed system, including recommendations for optimized loading methods categorized by part type and material. After the above steps are completed, the process should be undertaken that leads to development of a Technical Order for routine use of shearography at the depot level.

Thermal loading has obvious synergy with thermography. Simultaneous use of both methods should be complementary, and could be implemented as part of this development. Further analysis and design will be required to establish the potential of this "fused data" approach for extending the basic capability of the enhanced shearography system discussed here.

5.0 REFERENCES

(1) Y.Y. Hung, C.Y. Liang, "Image-Shearing Camera for Direct Measurement of Surface Strains", Appl Optics, Vol 18, No 7 (pp 1046–1051), April 1979

(2) H. Reismann, "Bending and Buckling of an Elastically Restrained Circular Plate", J. Appl. Mechanics, Vol 19, p. 167, 1952.

APPENDIX: SHEAROGRAPHY PRACTICAL IMPLEMENTATION GUIDE

A.1 General

This appendix addresses issues involved with practical implementation of shearography. There are limitations related to the user choice of the shearography camera subsystems (e.g., shearing angle, field of view (FOV)), and additional limitations imposed by the response to specific loading conditions of parts under inspection.

A fundamental limit on detectable flaw-size, is established by the shearing displacement projected onto the part. This displacement, Δ, is given by $\Delta = \alpha S$, where α is the shearing angle, and S is the distance between the camera and the part. Thus, if S = 24", and $\alpha = 0.5$ degrees (8.7 mrad), $\Delta = 0.2$". This would be the minimum detectable flaw size.

At the other end of the scale, the maximum detectable flaw is roughly the size of the FOV. This may be established by the camera FOV, or by external fixturing such as the frame of a vacuum box.

Analyses were completed for vacuum and vibration during this task, resulting in analytic expressions for part response to these loading methods. Although addressed, no similar analytic function was derived for the case of thermal loading. The response functions make it possible to establish parametric detection limits for unsupported sheets (such as debonds). These are discussed in the following.

A.2 Vacuum Excitation

Shearography inspectors quickly learn that shearography is not sensitive to small skin-to-core disbonds in composites with thick face sheets. This section discusses quantitative limits on disbond identification under the assumption that at least one full fringe count (2π phase) is required for recognition.

Shearographic sensitivity for normal illumination and viewing is given by Δ in equation A1.

$$\Delta = \left(\frac{4\pi}{\lambda}\right)\Delta x_o \frac{dw}{dx} \qquad (A1)$$

Δ = Relative phase change

λ = Wavelength of illuminating laser

Δx_o = Shearing distance (Shear angle * offset from part)

dw/dx = Surface slope

The slope, dw/dx, is calculated by differentiation of equation A2. The location of the maximum slope is calculated by setting the second derivative of equation A2 to zero resulting in equation A3. The maximum slope along the x-axis is then calculated from equation A4 by substituting the results of equation A3

$$w = \frac{q}{64D}\left(a^2 - r^2\right)^2 \qquad \text{(A2)}$$

$$Max\frac{dw}{dx}\ at\ r = \pm\frac{a}{\sqrt{3}} \qquad \text{(A3)}$$

$$\left(\frac{dw}{dx}\right)_{Max} = \frac{qa^3}{24\sqrt{3}\cdot D} \qquad \text{(A4)}$$

Substituting in equation A1, and setting $\Delta = 2\pi$, we arrive at an estimate for the minimum detectable flaw size. It is found to be linearly related to the face sheet thickness, h, for a given pressure differential, q. Note that it depends only on the 1/3 power of E/q, so that it is not greatly sensitive to material properties, or to loading pressure.

$$FlawSize = 2a = h\left\{2\left[\left(\frac{\sqrt{3}\cdot E}{2\left(1 - v^2\right)q}\right)\frac{\lambda}{\Delta x_o}\right]^{\frac{1}{3}}\right\} \qquad \text{(A5)}$$

Figure A1 shows a plot of equation A5 for selected loading pressures applied to aluminum. Figure 2 shows similar results for a typical quasi-isotropic composite. The graphs indicate the smallest flaw size that can be detected for any face sheet thickness, and excitation pressure. Flaw diameters above the lines can be detected. One can see that for a given face sheet thickness, the absolute minimum flaw size that can be detected is limited by the maximum attainable vacuum of 14.7 psi. For example, at this limit, the minimum disbond that can be observed in an aluminum bonded honeycomb structure with a 0.100 inch thick face sheet is 0.36 inch. In practice, typical applied pressure differentials are limited to about 2 psi or less. With this limitation, the minimum detectable flaw size is about 0.69 inch in the above example. These calculations use an illuminating laser operating at 532 nm, and a shearing distance of 0.25 inch (0.25 degree shearing angle at 24").

Note that there is very little difference in response between aluminum and a typical composite owing to the fractional power dependence on material properties.
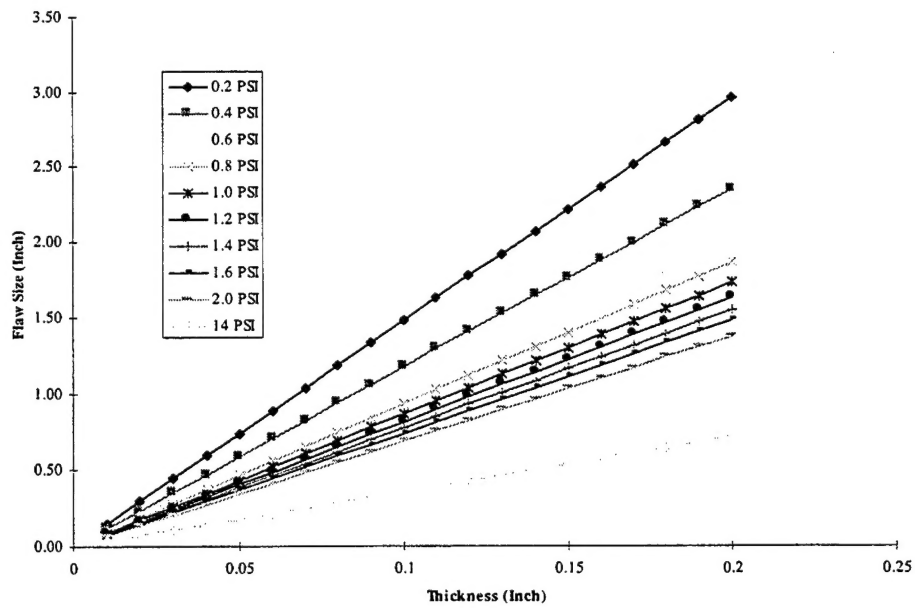
39

Figure A1.   Minimum detectable flaw size as a function of face sheet thickness for aluminum
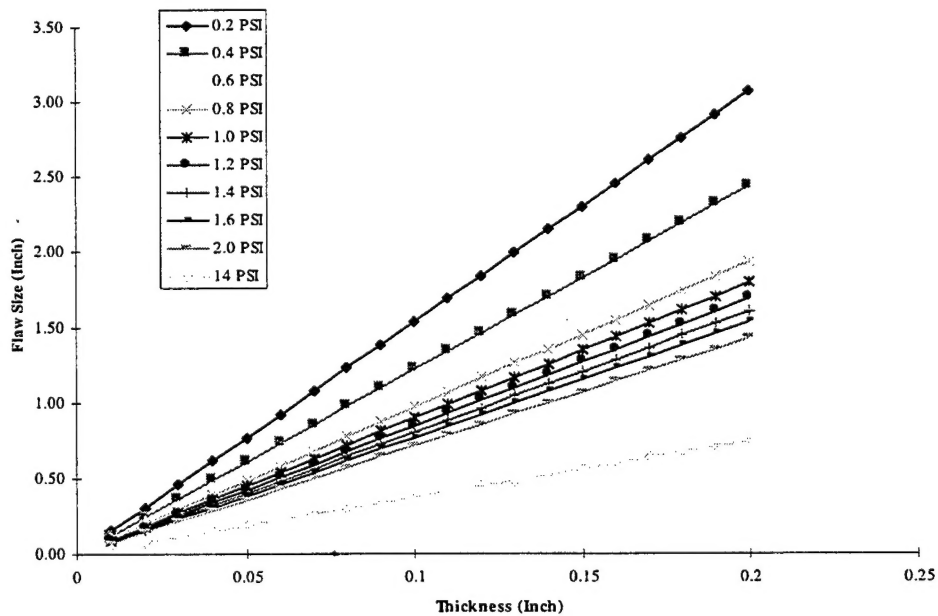

Figure A2.   Minimum detectable flaw size as a function of face sheet thickness for graphite/epoxy quasi-isotropic composite

A.3 Vibrational Excitation

This establishes the forcing frequency required to excite disbonds of a given size and face sheet thickness. The vibration frequency that excites the fundamental mode of a circular clamped plate is predicted by equation A6.

$$f = \frac{\lambda_1}{2\pi a^2}\sqrt{\frac{D}{\rho h}} \qquad (A6)$$

f = Fundamental frequency of defect modeled as clamped circular plate

λ_1 = Eigenvalue, for circularly clamped plate

a = Defect radius

D = Flexural rigidity $= \dfrac{Eh^3}{12(1-v^2)}$

h = Thickness

ρ = Mass density

Equation A7 represents the relationship between flaw size and disbond thickness, h, that will respond to a given forcing frequency, f. In this case, the flaw size varies as the square root of the disbond thickness, and material dependence is as the ¼ power. Thus, the relationship between flaw size and face sheet thickness will be very insensitive to material properties. Equation A7 shows that there is an approximately 11% difference between the outcomes for aluminum, and a typical graphite epoxy, even though their densities differ by a factor of nearly 2 (moduli are about the same). No assumption about the magnitude of the disbond response is included.

$$FlawSize = 2a = \sqrt{h}\left\{ \frac{\lambda_1}{\pi f}\left[\frac{E}{3\rho(1-v^2)} \right]^{\frac{1}{2}} \right\}^{\frac{1}{2}} \qquad (A7)$$

Figure A3 plots the results of equation A7, for aluminum, to establish a limit on detectable flaw size as a function of the disbond thickness for selected driving frequencies. Figure A4 is an equivalent graph for a typical composite. For example, if the flaw size is 0.75 inch diameter and the face sheet on the bonded aluminum honeycomb structure is 0.1 inch thick, then the shaker or speaker excitation must have a minimum capability of 65 kHz, which is higher than provided by commonly available equipment. A 0.5" disbond would be undetectable, even with a 65 kHz shaker. These graphs do not take into account the affects of the driving force magnitude or material damping on the maximum deflection of the defect. Consequently, driving a structure at the fundamental frequency of the defect of interest does not guarantee that sufficient amplitude will be present to detect the flaw.

This is a complex problem. Results depend very strongly on the equipment available for testing, and the specific test geometry. In general, a more uniformly distributed part excitation might be expected from a loud speaker, air-coupled to the part, than from a discretely located mechanical shaker which may not produce excitation at a particular defect location. On the other hand, the shaker would be expected to more efficiently couple power into the sample under test. The choice of excitation source must be determined for each application by trial and error, taking into account work-place environment considerations as part of the selection process.
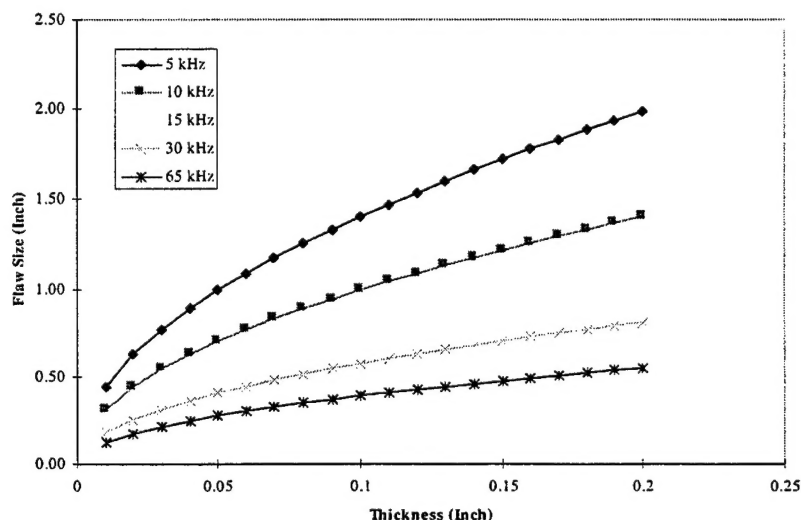

Figure A3.   Required forcing frequency for target flaw size and thickness for aluminum.
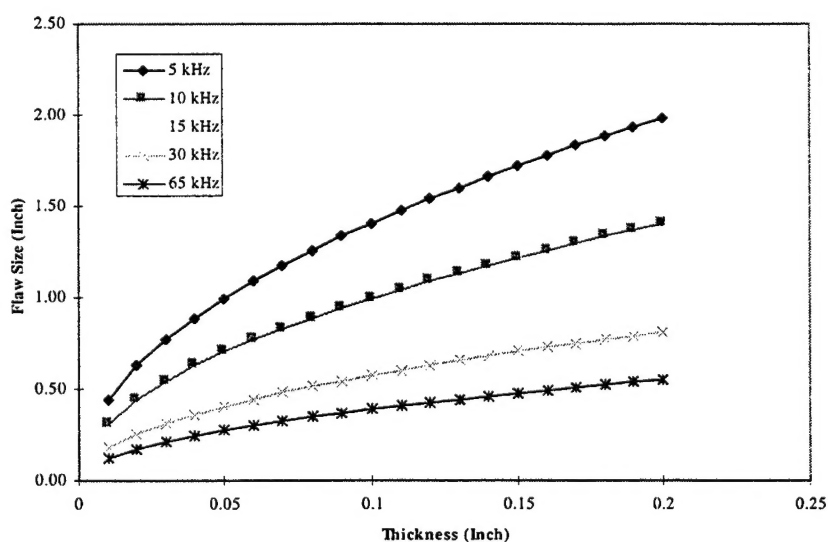

Figure A4.   Required forcing frequency for target flaw size and thickness for graphite/epoxy composite

A.4 Conclusions

The above graphs provide a useful guide for shearographic testing. Shearographic technicians are often asked to detect small flaws in thick materials. These results show that there are fundamental reasons why this can not be accomplished. Commercially available vibrational drivers often do not reach frequencies required for best detection probability. Boeing's 65 kHz driver is commercially available, but not in common usage. A more common commercial driver specifies a maximum frequency of 35 kHz. The graph shows the resultant detection limitations. Vibrational loading offers a potential for flaw dettections that can not be made with vacuum loading, but it must be remembered that it is not always easy to deliver adequate excitation amplitude at a flaw with vibrational drivers. Limitations include provision of adequate driving power at higher frequency, and the fact that a shaker excites vibrational mode patterns in parts under test that may have nodes at flaw locations.

Additional flaw size detection limitations are imposed, for small flaws, by the shearing offset associated with shearing angle and camera distance. The farther a camera is placed from a part, the larger the minimum detectable flaw size according to the relationship presented in section A.1. Large flaw detections are occasionally limited by the system FOV.